# Exploring the Impact of Volumetric Additive Manufacturing of Photo-crosslinkable Gelatin on Mesenchymal Stromal Cell Behavior and Differentiation

Nele Pien*, Bryan Bogaert, Marguerite Meeremans, Cezar-Stefan Popovici, Peter Dubruel, Catharina De Schauwer*, Sandra Van Vlierberghe*

N. Pien, B. Bogaert, M. Meeremans, C-S. Popovici, P. Dubruel, S. Van Vlierberghe: Polymer Chemistry and Biomaterials Group, Centre of Macromolecular Chemistry (CMaC), Department of Organic and Macromolecular Chemistry, Ghent University, Krijgslaan 281 building S4, 9000 Ghent, Belgium

N. Pien, M. Meeremans, C-S. Popovici, C. De Schauwer: Veterinary Stem Cell Research Unit, Department of Translational Physiology, Infectiology and Public Health, Faculty of Veterinary Medicine, Ghent University, Salisburylaan 133, 9280 Merelbeke, Belgium

Corresponding authors*:
Nele.Pien@ugent.be, Catharina.DeSchauwer@ugent.be, Sandra.VanVlierberghe@ugent.be

# Abstract

This study explores the application of photo-crosslinkable gelatin hydrogels (constituting GelSH and GelNB) for biofabrication using volumetric additive manufacturing (VAM). Three GelSH variants were prepared, yielding degree of substitutions (DS) of 39%, 54%, and 63%, and GelNB with a DS of 60%, alongside GelNB-GelSH formulations at concentrations of 5, 7.5, and 10% (w/v). Physico-chemical analyses confirmed that these variations led to differences in mass swelling ratio and mechanical properties. VAM enabled the fabrication of complex, high-fidelity 3D structures from the optimized GelNB-GelSH formulations, demonstrating its capacity to encapsulate mesenchymal stromal cells (MSCs) within a biomimetic matrix. Compared to the film casted constructs, the VAM-printed scaffolds exhibited significantly higher ALP activity and calcium deposition, confirming effective osteogenesis. Conversely, chondrogenic and adipogenic differentiation were more pronounced in the film casted groups due to their lower crosslinking density and lower compressive elastic modulus, emphasizing the role of the mechanical environment role in guiding cell differentiation. This study highlights the potential of VAM to produce complex and functional hydrogel scaffolds for tissue engineering, and lays the groundwork for future work on finetuning bioresin formulations to enhance differentiation across multiple lineages for various tissue engineering applications, including softer tissues.



**Keywords:** tomographic volumetric additive manufacturing; photo-crosslinkable gelatin; bioresin development; mesenchymal stromal cells; MSC differentiation; cell-biomaterial interactions.

# Table of Contents

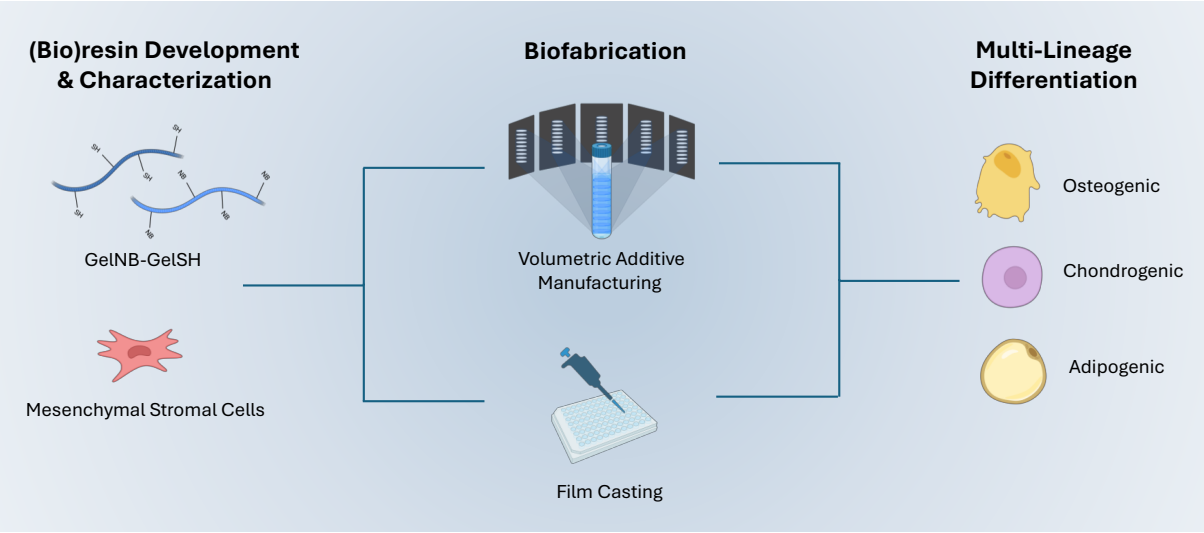


This study investigates photo-crosslinkable gelatin hydrogels (GelSH and GelNB) for volumetric additive manufacturing (VAM) in biofabrication. Different formulations influenced swelling and mechanical properties. VAM produced complex 3D scaffolds encapsulating mesenchymal stromal cells, enhancing osteogenesis compared to film-cast constructs. The findings highlight VAM's potential for tissue engineering and optimizing bioresins for multi-lineage differentiation, including softer tissues.

# 1. Introduction

Biofabrication, the creation of 3D biological structures, has emerged as a transformative approach in tissue engineering, offering promising solutions for creating functional tissues and organs serving regenerative medicine.[1] This field combines advanced manufacturing technologies with biological materials, aiming to replicate the complexity and functionality of native tissues.[2,3] The ability to precisely control both the material properties and the geometry of tissue scaffolds is crucial for successful tissue regeneration, as the mechanical and biological properties of the scaffolds directly influence cellular behavior and tissue development. As such, the development of new materials and innovative fabrication techniques is at the forefront of biofabrication research.

Volumetric additive manufacturing (VAM) is a novel 3D printing technique that represents a significant advancement over traditional layer-by-layer methods.[4] Unlike deposition-based 3D printing, which is limited by the sequential addition of layers, VAM utilizes light to polymerize a material throughout an entire volume simultaneously, enabling the rapid production of highly detailed, intricate, and complex 3D structures in a single step.[4–6] Several volumetric light-based techniques have been developed showing unprecedented short printing times (down to a few tens of seconds) [7], while achieving good resolution (down to tens of micrometers, i.e., 20 µm)[8] and accuracy, making it ideal for creating scaffolds that mimic the architecture and function of native tissues.[9,10] The use of light-based polymerization in VAM also allows for fine control over the curing process, which is essential for creating well-defined scaffold features that promote cellular infiltration and tissue integration.[9,11]

For tissue engineering applications, hydrogels are particularly attractive due to their biocompatibility, high water content, and ability to mimic the extracellular matrix (ECM) of tissues.[12] However, the incorporation of photocrosslinkable functionalities into hydrogel building blocks is critical to enable precise control over their gelation process and mechanical properties during fabrication.[13] Among the various methods of crosslinking, the thiol-ene click-like reaction between norbornene-modified gelatin (GelNB) and thiolated gelatin (GelSH) has proven to be particularly effective.[14,15] This reaction is highly efficient, occurs under mild conditions, and allows for rapid crosslinking under light exposure (in the presence of a suitable photo-initiator).[16–18] The fast crosslinking kinetics offered by the thiol-ene reaction are especially beneficial for VAM, where quick and uniform polymerization is required to achieve high-resolution prints.[19] Furthermore, gelatin, a biopolymer derived from collagen, is an excellent choice for biofabrication due to its inherent bioactivity, biodegradability, and ability to support cell adhesion and growth.[20]

In tissue engineering, selecting appropriate materials and processing techniques is crucial, as these factors directly impact the scaffold's biological and mechanical properties. The scaffold's mechanical properties, such as stiffness and elasticity, must be tailored to meet the specific needs of the targeted tissue.[21,22] Likewise, the material's ability to support cellular interactions and guide cell behavior is equally important.[23,24] These material-processing interactions are particularly crucial when working with stem cells, such as mesenchymal stromal cells (MSCs), which are capable of differentiating into a variety of tissue types, including bone, cartilage, and adipose tissue.[25,26] MSCs respond to mechanical cues and scaffold architecture to direct their differentiation. [21,27] Prior research has demonstrated that MSCs tend to differentiate into osteoblasts in stiffer substrates [28,29], e.g. a E-modulus between 11 and 30 kPa has been shown to promote osteogenic differentiation [30], whereas softer substrates promote adipogenic differentiation (E = 2 kPa) [31]. This illustrates that it is essential to carefully design scaffolds with the appropriate combination of material properties and processing techniques.[32–34]

The aim of this study is to investigate how VAM biofabrication of GelNB-GelSH hydrogels influences MSC proliferation and differentiation, providing insights into stem cell fate and advancing the use of VAM to serve tissue engineering applications.

# 2. Materials and methods

## 2.1 Materials

1-(3-Dimethylaminopropyl)-3-ethylcarbodiimide hydrochloride (EDC•HCl, TCI Europe, D1601, 25952-53-8, Zwijndrecht); 2-mercaptoethanol (TCI Europe, M0058, 60-24-2, Zwijndrecht), 3-(4,5-dimethylthiazol-2-yl)-5-(3-carboxymethoxyphenyl)-2-(4-sulfophenyl)-2H-tetrazolium (MTS, Abcam, ab197010, 138169-43-4, Cambridge); 4-nitrophenyl phosphate (pNPP, ThermoFisher, 455010100, 330-13-2, Pittsburgh); 5-norbornene-2-carboxylic acid (Merck, 446440, 120-74-1, Darmstadt); (alcian blue, Merck, A3157, 33864-99-2, Darmstadt); alkaline phosphatase (ALP, Sigma, P7640, 9001-78-9, Darmstadt); boric acid ($H_3BO_3$, Merck, B6768, 10043-35-3, Darmstadt); calcein acetoxymethyl ester (Ca-AM, Merck, 56496, 148504-34-1, Darmstadt); calcium chloride ($CaCl_2$, Sigma, C1016, 10043-52-4, Darmstadt); collagenase (ThermoFisher, 17100017, 9001-12-1, Pittsburgh); cresolphthalein (Sentinel Diagnostics, 17667H, 596-27-0, Milan); deuterium oxide ($D_2O$, Eurisotop, D214H, 7789-20-0, Saint-Aubin); dialysis membrane (SpectraPor, MWCO 12-14 kDa, VWR, 734-0681, N/A, Pennsylvania); dimethyl sulfoxide (DMSO), Chem-Lab, CL00.0422.2500, 67-68-5, Zedelgem); ultrapure water (Milli-

Q); Dulbecco's phosphate buffered saline (DPBS, ThermoFisher, 14190250, N/A, Pittsburgh); ethanol (EtOH, Chem-Lab, CL00.0529.2500, 64-17-5, Zedelgem); ethylenediaminetetraacetic acid tetrasodium salt tetrahydrate (EDTA•4 $H_2O$, Merck, 34103, 13235-36-4, Darmstadt); fetal bovine serum (FBS, Merck, F7524, 9014-81-7, Darmstadt); Fluorobrite™ DMEM (Fluorobrite™, ThermoFisher, A1896701, N/A, Pittsburgh); gelatin type B (Rousselot, , 9000-70-8, Ghent); guanidine•HCl (Carl Roth, 0037.3, 50-01-1, Karlsruhe); hydrogen chloride (HCl, Merck, 258148, 7647-01-0, Darmstadt); iodixanol (OptiPrep™, StemCell Technologies, 7820, 92339-11-2, Vancouver); isopropanol (IPA, Merck, 190764, 67-63-0, Darmstadt); L-glutamine solution (Merck, 25030024, 56-85-9, Darmstadt); low glucose Dulbecco's modified eagle medium (Lg-DMEM, ThermoFisher, 11880028, N/A, Pittsburgh); N-acetyl-homocysteine thiolactone (Merck, A16602, 1195-16-0, Darmstadt); n-butylamine (Acros Organics, 219742500, 109-73-9, Geel); N-hydroxysuccinimide (NHS, Merck, 130672, 6066-82-6, Darmstadt); o-phthalaldehyde (OPA, Merck, P1378, 643-79-8, Darmstadt); Oil Red O (Merck, O0625, 1320-06-5, Darmstadt); Paraformaldehyde (Merck, 441244, 30525-89-4, Darmstadt); penicillin-streptomycin-amphotericin B suspension (ABAM, Merck, A5955, N/A, Darmstadt); phenylmethylsulfonyl fluoride (PMSF, Merck, 10837091001, 329-98-6, Darmstadt); phosphate buffered saline (PBS, Merck, P4417, N/A, Darmstadt); potassium chloride (KCl, Merck, 746436, 7447-40-7, Darmstadt); propidium iodide (PI, ThermoFisher, 15438249, 25535-16-4, Pittsburgh); PTFE-based release foil (ACC-3, Ventec International group); reverse osmosis water (Milli-RO); sodium bicarbonate ($NaHCO_3$, TCI Europe, S0561, 144-55-8, Zwijndrecht); sodium carbonate ($Na_2CO_3$, TCI Europe, S0560, 497-19-8, Zwijndrecht); sodium hydroxide (NaOH, Merck, 221465, 1310-73-2, Darmstadt); tris(hydroxymethyl)aminomethane hydrochloride salt (TRIS•HCl, Merck, 10812846001, 1185-53-1, Darmstadt); triton X-100 (Merck, X100, 9036-19-5, Darmstadt); trypsin-ethylenediaminetetraacetic acid (Trypsin-EDTA, Merck, T4049, N/A, Darmstadt)

## 2.2 Development of photo-crosslinkable biomaterials

For the synthesis of thiolated gelatin (GelSH, Figure S1), a slightly adapted protocol from Meeremans *et al.* [35] was followed, employing three different molar ratios of amine to N-acetyl homocysteine thiolactone (1:1, 1:3, and 1:5) to achieve low, medium, and high degrees of substitution (DS). Gelatin-norbornene (GelNB, Figure S2) targeting a DS of 60%, was synthesized following a previously reported protocol [21]. The process involved activating 5-norbornene-2-carboxylic acid with EDC·HCl and NHS in DMSO, followed by conjugation to gelatin type B under inert conditions at 50°C for 16 hours. The product was purified through precipitation, dialysis, and lyophilization to obtain the final GelNB.

## 2.3 Characterization of developed photo-crosslinkable materials

### *2.3.1 $^1$H-NMR spectroscopy*

The number of functional end groups in GelNB was determined using proton nuclear magnetic resonance ($^1$H-NMR) spectroscopy [21]. In brief, 10 mg of the material was dissolved in 1 mL of deuterium oxide ($D_2O$) and analyzed on a Bruker Avance WH 500 MHz NMR spectrometer at 40°C. The characteristic peaks of norbornene (6.0 and 6.3 ppm) were compared with the reference peak of the chemically inert hydrogen atoms of Valine (Val), Leucine (Leu), and Isoleucine (Ile) at 1.01 ppm. The NMR spectra were further analyzed using MestreNova software (version 6.0.2-5475), with baseline correction performed using the Whittaker smoother method. The following equations were used to calculate the DS for GelNB:

$$n_{norbornene} = n_{methyl\ protons} \cdot \frac{\frac{(I_{6.0} + I_{6.3})}{2}}{I_{1.0}} \quad (1)$$

$$DS\ [\%] = \left(\frac{n_{norbornene}}{n_{NH_2}}\right) \cdot 100\% \quad (2)$$

With:

$I_{d\ =\ 6.3\ -\ 6.0\ ppm}$ = integral of the signal of the protons of norbornene
$I_{d\ =\ 1.0\ ppm}$ = integral of the signal of the protons of the reference peak
$n_{NH_2}$ = 0.0385 moles primary amines per 100 g gelatin type B
$n_{methyl\ protons}$ = 0.384 moles methyl protons (in reference signal) of Val, Leu and Ile per 100 g gelatin type B

### *2.3.2 OPA assay to determine the degree of substitution of GelNB and GelSH*

The number of functional end-groups in GelSH and GelNB was quantified using an o-phthalaldehyde (OPA) assay as previously described [36]. In brief, gelatin solutions were reacted with OPA and 2-mercaptoethanol, and the absorbance was measured at 335 nm via UV-VIS spectroscopy, with a blank for reference. A calibration curve with n-butylamine standards was used to calculate the degree of substitution based on the amount of unreacted amine groups.

### *2.3.3 Preparation of solutions for photorheology and crosslinking of sheets*

A stock solution of 0.8% (w/v) lithium phenyl-2,4,6-trimethylbenzoylphosphinate (LAP) was prepared by dissolving 40 mg of LAP in 20 mL of ultrapure water. An aqueous solution of GelSH (1, 3 or 5 eq) and GelNB was prepared using an equimolar ratio of thiol to alkene functionalities (GelNB-GelSH concentration of 5%, 7.5% and 10% (w/v)). Upon complete dissolution, 2 mol% (corresponding to 0.0076% (w/v)) of LAP was added with respect to the -NB functionalities. These mixtures were then used for comparative photorheology measurements and to prepare hydrogel films.

### *2.3.4 In situ crosslinking using photorheology*

The UV-crosslinking behavior of the aforementioned materials was analyzed using photorheology with an Anton Paar Physica MCR 302e rheometer. The rheometer was equipped with an Omnicure S1500 light source, featuring a filter for wavelengths between 400–500 nm, which irradiated the sample from below through a quartz plate. A parallel plate setup with a 25 mm diameter top spindle was utilized. The curing process was monitored by deriving the storage modulus (G') and loss modulus (G'') of the solutions over time under light exposure (22.5 $mW \cdot cm^{-2}$) at 37°C, with a strain of 0.1% and a frequency of 1 Hz to ensure measurements were within the linear viscoelastic range. The initial gap between the plates was set to 0.300 mm, and the normal force was maintained at 0.5 N throughout the experiment. Measurements of the storage and loss moduli were taken before, during, and after light irradiation with interval durations of respectively 1 minute, 9 minutes, and 5 minutes.

### *2.3.5 Photocuring of the solutions to prepare hydrogel films*

The solutions (as described in section 2.3.3) were placed between two parallel glass plates that were covered with PTFE-based release foil and separated with a 1 mm thick silicone spacer. The material was then irradiated for 30 minutes from top and bottom with UV-A light (λ = 320-380 nm, 2 × 4 $mW \cdot cm^{-2}$) to ensure complete crosslinking. LAP has a local absorbance maximum at approximately 375 nm and significant absorbance at 365 nm (molar extinction coefficient at 365, ε=218 $M^{-1}cm^{-1}$).[37]

### *2.3.6 HR-MAS $^{1}$H-NMR spectroscopy*

The absolute crosslinking efficiency can be determined via high resolution magic angle spinning (HR-MAS) NMR spectroscopy [38]. Measurements were conducted on a Bruker Ascend™ 500 MHz spectrometer with a 4 mm $^{1}H/^{13}C$ dual-channel HR-MAS probe at r.t. and a 6 kHz spinning rate. Freeze-dried samples were compressed in Kel-F inserts with 45 µL $D_2O$, sealed, and placed in the rotor. Quantitative data were obtained with a 30-second relaxation time, and the degree of conversion (DC) was calculated using the following equation:

$$DC\ [\%] = \frac{\frac{I_i}{I_{ri}} - \frac{I_e}{I_{re}}}{\frac{I_i}{I_{ri}}} \cdot 100 \qquad (3)$$

$I_i$ = integral of the norbornene before crosslinking (6.0 – 6.3 ppm)
$I_{ri}$ = integral of the reference peak before crosslinking (1 ppm)
$I_e$ = integral of the norbornene after crosslinking (6.0 – 6.3 ppm)
$I_{re}$ = integral of the reference peak after crosslinking (1 ppm)

### *2.3.7 Evaluation of the gel fraction and mass swelling ratio*

Cylindrical samples (diameter: 6 mm, thickness: 1 mm) were punched out of the hydrogel films (see 2.2.5). The samples were lyophilized and weighed in dry state to determine the dry mass ($m_{d1}$). Next, the samples were incubated in ultrapure water at 37°C for 72 hours, the mass was recorded ($m_s$) and the discs were lyophilized once more to determine the second dry mass ($m_{d2}$). The gel fraction and mass swelling ratio q were then calculated using the following equations:

$$Gel\ fraction\ [\%] = \frac{m_{d2}}{m_{d1}} \cdot 100 \tag{4}$$

$$Mass\ swelling\ ratio\ q\ [-] = \frac{m_s}{m_{d2}} \tag{5}$$

### *2.3.8 Frequency sweep of crosslinked hydrogel samples*

The viscoelastic properties of the materials were determined by a frequency sweep analysis. This was performed with a Physica MCR 301 rheometer from Anton Paar equipped with a plate with diameter of 15 mm. First, hydrogel films were prepared according to section 2.3.5. The films were subsequently swollen to equilibrium in ultrapure water at room temperature for 72 hours. After reaching complete swelling, cylindrical samples of 14 mm were punched out. A frequency sweep analysis was performed from 0.1 to 10 Hz ($F_N$ = 0.5 N, amplitude of 0.1% and T = 37°C) to determine the storage (G') and loss (G'') moduli. The compressive modulus (E) was then calculated using the following equation:

$$E = 2 \cdot G'(1 + \nu) \tag{6}$$

Where $\nu$ is the Poisson number assumed to be 0.5 for ideal hydrogels.[30]

### *2.3.9 Tensile testing on crosslinked ring-shaped hydrogel samples*

Hydrogel films were produced as described in section 2.3.5. Rings of 14 mm inner diameter and 18 mm outer diameter with a thickness ≈ 1.5 mm were punched out. The tensile properties of the equilibrium swollen GelNB-GelSH samples were determined at room temperature using a universal testing machine (Tinius Olsen 3ST) equipped with a 500 N load cell. The specimens were positioned as shown in Figure 1, between two 3D-printed curved hooks with a diameter of 5 mm. This method was developed specifically for gelatin-based hydrogels, instead of the traditional dogbone-shaped samples, that encounter issues when gelatin-based hydrogels are clamped between the grips.

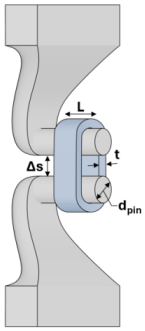


*Figure 1. Tensile testing setup for hydrogel rings: Samples were mounted between 3D-printed curved hooks ($d_{pin}$ = 5 mm) and tested using a universal testing machine. A preload force of 0.01 N was applied, and specimens were stretched at 5 mm·min$^{-1}$. Displacement (Δs) was used to calculate the internal circumference (C), strain (ε), and circumferential stress (σ), where $d_{pin}$ is the hook diameter, L is the specimen length, and t is the specimen thickness. Young's modulus was determined from the linear region of the stress-strain curve.*

A preload force of 0.01 N was applied and the specimens were tested at a crosshead velocity of 5 mm·min$^{-1}$. From this, the displacement and force were measured and transformed into stress-strain plots. Using the displacement, $\Delta_s$, the internal circumference, C, was calculated using the following formula:

$$C = d_{pin}(\pi + 2) + 2\Delta_s \tag{7}$$

where $d_{pin}$ is the diameter of the 3D-printed hooks. The circumferential stress, σ, and the strain, ε, were calculated as the ratio of C with the initial internal circumference, $C_{init}$, using the following formulas:

$$\varepsilon = \frac{C - C_{init}}{C_{init}} \tag{8}$$

$$\sigma = \frac{F}{2Lt} \tag{9}$$

where F is the applied load during testing and L and t are the length and thickness of tubular specimen. Young's moduli were calculated from the initial linear region slope of the stress-strain plots.

## 2.4 Photoresin preparation and characterization

### *2.4.1 Preparation of the photoresins*

Aqueous solutions of GelSH5eq and GelNB in ultrapure water were prepared using an equimolar ratio of thiol to alkene. Upon complete dissolution, LAP stock solution was added to yield a final LAP concentration of 0.05% (w/v) and a final total gelatin concentration of 10% (w/v).

### *2.4.2 Determination of gel point for dose optimization*

Photorheology was performed to gain insight in the crosslinking kinetics as well as the optimal dose for volumetric printing. The photorheology analysis was performed as described in section 2.3.4 aside for a reduction of light intensity in order to increase the accuracy by delaying the cross-over point. The dose used as reference dose for volumetric printing ($D_v$) was calculated using the following formula:

$$D_v \left[\frac{mJ}{cm^2}\right] = T_{gel\ point}[s] \cdot D_r \left[\frac{mW}{cm^2}\right] \tag{10}$$

where Dr is the light dose used for photorheology and $T_{gel\ point}$ is the time in seconds from the start of the light irradiation until the G'-G" crossover as shown in Figure S3.

### *2.4.3 Absorption coefficient*

The absorbance at 405 nm was measured using UV-VIS spectroscopy (UvikonXL, Bio-Tek Instruments) equipped with a temperature control unit. The temperature was set to 4°C and allowed to equilibrate for 30 minutes. The resins were prepared as described in section 2.4.1. Subsequently, 500 µL was transferred to a PMMA micro-cuvette avoiding any entrapped air bubbles. The cuvette was inserted into the cooled spectrophotometer chamber and the absorbance of the sample was recorded after 7 minutes. The absorption coefficient $\alpha(\lambda)$ used for volumetric printing (Tomolite v1.0) was calculated using Equation 11, where $A(\lambda)$ is the absorbance measured with the spectrophotometer, and t is the thickness of the sample:

$$\alpha(\lambda)[cm^{-1}] = 2.303 \frac{A(\lambda)}{t\ [cm]} \tag{11}$$

### *2.4.4 Measuring the refractive index*

The refractive index (RI) of the photo-bioresins were measured by applying 300 µL of the resin on the sensor of the refractometer (Deosdum). The refractometer was then placed in the fridge (4°C) for 7 minutes after which the RI was determined.

### *2.4.5 Dose testing*

The dose testing followed the Readily3D protocol. In brief, 3 mL of the resin was added to the cuvette, placed in a cuvette holder, stored in the fridge for 7 minutes and inserted into the Tomolite printer. Next, the resin was exposed to 25 different dose levels, by varying both time and intensity. Each exposure was delivered in the form of an 800 µm diameter spot with a 1 mm gap between spots and a bottom margin of 4 mm. The diameters of the exposed spots were measured using optical light microscopy (Zeiss-Axiotech100HD/DIC) with ZEN Core software. The classification of the exposed

spots was conducted based on four categories: "No dot" (invisible to the naked eye or under a microscope), "Barely visible" (if $D_{spot}/D_{expected} < 0.625$ or visible to the naked eye), "Small" (if $0.75 > D_{spot}/D_{expected} > 0.625$), and "Large" (if $D_{spot}/D_{expected} > 0.75$), where $D_{spot}$ is the measured diameter [µm] and $D_{expected}$ is the set diameter [800 µm]. The optimized dose was determined as the last, fully printed isodose of this dose test. The optimized dose D was calculated using Equation 11.

$$D\left[\frac{mJ}{cm^2}\right] = I\left[\frac{mW}{cm^2}\right] \cdot t[s] \tag{12}$$

where *I* represents the intensity and *t* the illumination time.

## 2.5 Volumetric printing

### *2.5.1 Scaffold design*

Four different designs were VAM-printed (Figure 4), for various testing purposes. To determine the printing resolution of the resins, a Schoen I-graph-wrapped package (IWP) was printed (Figure 4.A). Moreover, the CAD/CAM mimicry was evaluated on the benchmark from Figure 4.B, designed in Blender 4.0 graphical software with features ranging in sizes that challenge different aspects of printing resolution (positive vs negative resolution and z-axis vs x- and y-axis). For compression testing, cubes (dimensions: 5 mm x 5 mm x 5 mm) were printed, whereas discs (diameter of 8.8 mm and height of 1.5 mm) were printed for rheological measurements (frequency sweep analysis), as depicted in Figures 4.C and D respectively.

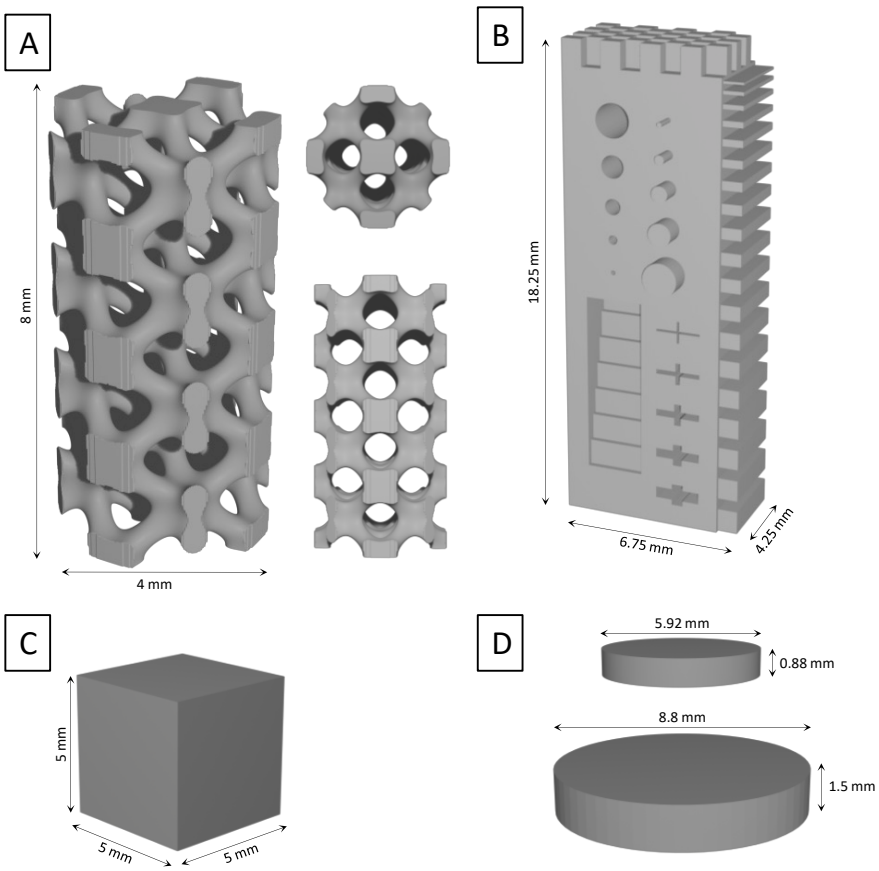

*Figure 2. Designs that were volumetrically printed in this work for characterization of the scaffolds: (A) IWP design; (B) Benchmark 3D model for evaluation of the printing resolution and CAD/CAM mimicry; (C) Cubes (5x5x5 mm³) for compression testing; (D) Discs (diameter 8.8 mm and height 1.5 mm) for frequency sweep analysis (top) and discs with a diameter 5.25 mm and height 0.88 mm for cell encapsulation (bottom).*

### *2.5.2 Volumetric printing process*

Resins were prepared according to section 2.3.1 and transferred to vials, ensuring no entrapped air bubbles were present. The vials were then placed in the fridge at 4°C for 7 minutes, before being transferred to the printing chamber of the volumetric printer. The STLs (depending on the purpose of the experiment) were loaded, and the parameters were set as follows; dose: 56 $mJ \cdot cm^{-2}$, refractive index: 1.334, voxel size: 25 µm. Once the printing process was complete, the vials were left in the printing chamber for 1 minute to allow for dark crosslinking.

### *2.5.3 Post-printing processing*

The vials were removed from the printing chamber and placed in a hot water bath (37°C) until the resin liquified (30 - 90 seconds). The liquified resin with printed structures was then poured into pre-heated PBS and washed for 2 minutes. Finally, the structures were transferred to a well plate, fresh PBS was added, and they were post-cured under UVA light or 405 nm light source (5, 10 or 15 minutes). The intensity of the light source was set at 8 $mW \cdot cm^{-2}$. Then, the double bond conversion percentage was assessed by HR-MAS NMR measurements (as described in section 2.3.6). A VAM-printed sample without post-processing curing was used as a negative control.

### *2.5.4 CAD/CAM mimicry*

The benchmark (Figure 4.B) was printed using the protocol from section 2.5.2. Optical light microscopy (Zeiss-Axiotech100HD/DIC) with ZEN Core software was used to measure the features immediately after the washing step. The dry state of the volumetrically printed scaffolds was visualized by scanning electron microscope (SEM, JCM-7000). Prior to SEM analysis, the samples were gold coated by sputter coating for 60 seconds at 15 mA under vacuum (K550X EmiTech).

### *2.5.5 Mechanical characterization*

#### *a) Compression testing on volumetrically printed cubes*

To conduct the compression test of the 3D printed hydrogels, cubes of 5x5x5 $mm^3$ were VAM-printed following the protocol described in section 2.5. The cubes were then allowed to swell to equilibrium in ultrapure water for 72 hours at 37°C and were tested until failure at a compression rate of 2 $mm \cdot min^{-1}$ with a preload force of 0.01 N (Tinius Olsen 3ST).

*b) Frequency sweep on volumetrically printed discs*

To conduct oscillatory rheology of the VAM-printed hydrogels, discs with a diameter of 8.8 mm and a height of 1.5 mm were printed as described in section 2.5. The discs were allowed to swell to equilibrium in ultrapure water for 72 hours at 37°C and analyzed as described in section 2.3.8.

## 2.6 Volumetric bioprinting with mesenchymal stromal cells

### *2.6.1 Cell isolation and culture*

Equine adipose tissue-derived MSCs were cultured under standard culture conditions, i.e. 38°C, 5% $CO_2$, in expansion medium containing 20% FBS (Table 1). When a confluency of 80% was reached, cells were enzymatically detached with trypsin-EDTA (0.25% (w/v) trypsin, 0.53 mM EDTA) and counted. Cells of passage 4 were used for the experiments.

### *2.6.2 Preparation of the photo-bioresin*

For volumetric printing with MSCs, a solution of the GelNB-GelSH5eq in DPBS was prepared. Iodixanol (OptiPrep™, STEMCELL Technologies) stock solution (60%) was added to the GelNB-GelSH mixture to afford a final concentration of 0, 10, 15, or 20% (v/v) OptiPrep™, to tune the refractive index (RI) of the resin to that of the cell cytoplasm to avoid undesired scattering and print defects [39,40] – the RI was measured as described in section 2.4.4. Lastly, LAP stock solution (0.8% (w/v) LAP in DPBS) was added to yield a final concentration of gelatin of 10% (w/v) and a final LAP concentration of 0.05% (w/v). Upon complete dissolution, the solution was homogeneously mixed with MSCs (2 million cells·$mL^{-1}$, passage 4). The various photoresins were characterized by photorheology, UV-VIS spectroscopy, refractometry (see section 2.4).

### *2.6.3 Parameters for volumetric bioprinting with MSCs*

Two designs were VAM bioprinted: (1) disc (0.88 mm thickness, 5.28 mm diameter - which will result, after equilibrium swelling, into a disc with dimensions: 1 mm thickness and 6 mm diameter) and (2) the IWP structure (at 20% from the original .STL file). Volumetric printing was performed using the protocol from section 2.5.1. The post-processing curing consisted of 5 minutes under 405 nm light. The printed samples were then moved to a 96- or a 24-well plate, respectively. Expansion medium (100 µL or 1 mL) was added to each well, respectively. The medium was changed twice weekly.

## 2.7 Biological characterization of encapsulated MSCs

### *2.7.1 Cell encapsulation in casted film versus VAM-printed scaffolds*

For the MSC encapsulation within a GelNB-GelSH hydrogel (later referred to as casted film), and to evaluate the biological properties of the hydrogel itself: A 10% (w/v) GelNB-GelSH63 was prepared as described in Section 2.3.3. Upon dissolution, the gelatin solution was homogeneously mixed with MSCs at a concentration of 2 million cells·mL$^{-1}$. Then, 100 µL of this solution was pipetted in a 96-well plate. The cell-laden samples were placed in the fridge (10 min) for physical gelation, followed by 10 minutes of UV-A irradiation, as described earlier.[30] For the volumetric printing of the bioresin, and to evaluate the effect of the VAM printing process on the encapsulated MSCs, a GelNB-GelSH5eq (10% (w/v), 0.05% (w/v) LAP) solution was prepared in DPBS with 15% (v/v) OptiPrep™. Then, 2 million MSCs·mL$^{-1}$ were homogeneously mixed in and transferred to the VAM vial. The VAM printing was performed as described in section 2.6.3.

### *2.7.2 Viability and proliferation assay*

A 3-(4,5-dimethylthiazol-2-yl)-5-(3-carboxymethoxyphenyl)-2-(4-sulfophenyl)-2H-tetrazolium (MTS) assay was performed in order to assess the MSC metabolic activity. The expansion medium was removed and replaced with 120 µL MTS solution, i.e. 100 µL LG-DMEM and 20 µL MTS reagent. After an incubation period of 2 hours in the dark, the absorbance was measured using a plate reader (Multiskan SkyHigh Microplate Spectrophotometer, ThermoFisher Scientific) at 490 and 750 nm (as background). The MTS assay was performed on days 1, 7, 14 and 21 (n = 3). The hydrogel (without cells) was used as a control group.

A live/dead staining was performed using a dye solution of calcein acetoxymethyl (Ca-AM) and propidium iodide (PI) in Fluorobrite™ DMEM to visualize the living and dead cells, respectively. The viability assay was also performed on days 1, 7, 14 and 21 (n = 3). The hydrogel (without cells encapsulated) was used as control group. On the evaluation days, the expansion medium was removed, and samples were washed twice with DPBS. Then, the dye solution containing 2 µL·mL$^{-1}$ Ca-AM and 2 µL·mL$^{-1}$ PI in Fluorobrite™ DMEM was added to each sample (100 µL). After an incubation period of 15 minutes in the dark at room temperature, the dye solution was removed, the discs were washed with DBPS and Fluorobrite™ DMEM was added. Then, (z-stack) imaging was performed using an inverted microscope (DMi1, Leica Biosystems). The raw data images were exported, and Fiji software version 2.9.0 was used to calculate the live/dead ratio.

### *2.7.3 Preparation of media*

The composition of the expansion medium (undifferentiated MSCs, CTRL) and the adipogenic, osteogenic and chondrogenic media (later referred to as differentiation media, DIFF) is provided in Table 1. To induce adipogenic differentiation, the encapsulated MSCs in GelNB-GelSH scaffolds were cultured in adipogenic induction medium for 72h, altered by 24h in adipogenic maintenance medium until analysis at day 21. For osteogenic and chondrogenic differentiation, the encapsulated MSCs were cultured up to 21 days.

*Table 1. Composition of media used for expansion (CTRL) and induction (DIFF).*

| Expansion medium | Adipogenic Induction | Adipogenic Maintenance | Osteogenic | Chondrogenic |
|---|---|---|---|---|
| DMEM-LG (Invitrogen, 11880-028) | DMEM-LG (Invitrogen, 11880-028) | DMEM-LG (Invitrogen, 11880-028) | DMEM-LG (Invitrogen, 11880-028) | Basal differentiation medium (Lonza, PT-3925) |
| 10% FBS | 15% rabbit serum (Sigma, R4505) | 15% rabbit serum (Sigma, R4505) | 10% FBS | |
| - 1% = 2mM glutamine (Gibco, 25030024)<br>- 1% ABAM (Sigma, A5955) | - 1 µM dexamethasone (Sigma, D2915)<br>- 1% ABAM (Sigma, A5955) | - 10 µg·mL$^{-1}$ rh-insulin (Sigma, I9278)<br>- 1% ABAM (Sigma, A5955) | - 100 nM dexamethasone (Sigma, D2915)<br>- 10 mM β-glycerophosphate (Sigma, G9422)<br>- 0.05 mM L-ascorbic acid-2-phosphate (Fluka, 49752)<br>- 1% ABAM (Sigma, A5955) | - Single Quots differentiation medium (Lonza, PT-4121)<br>- 10 ng·mL$^{-1}$ Transforming Growth Factor-β3 (Sigma, T5425) |

### *2.7.4 Differentiation assays*

To assess alkaline phosphatase (ALP) activity, an early marker of osteogenesis, triplicate samples were washed with DPBS after 7 and 21 days of osteogenic differentiation and digested for 2 hours using 200 µL of collagenase suspension (1 mg·mL$^{-1}$) per sample. Following digestion, 150 µL of lysis buffer (consisting of 0.2% Triton X100 (Merck), 10 mM Tris•HCl at pH 8, and 0.5% phenylmethylsulfonyl fluoride (PMSF) in ultrapure water) was added. An 8-point standard curve was constructed by mixing 120 µL of p-nitrophenyl phosphate (pNPP) at varying concentrations (0–80 nmol·well$^{-1}$) with 10 µL of ALP solution (1 mg·mL$^{-1}$). Next, 80 µL of the diluted cell lysates were combined with 50 µL of pNPP solution. If necessary, further dilutions of the cell lysates were prepared to ensure the results fitted within the range of the standard curve. The absorbance was measured at 405 and 750 nm (Multiskan SkyHigh Microplate Spectrophotometer). ALP activity was then calculated as:

$$ALP\ activity\ \left[\frac{nmol}{ml \cdot min}\right] = \frac{A}{V\ x\ t} \tag{13}$$

where A represents the amount of p-nitrophenol (pNP) produced (nmol), V is the volume of cell lysate added to the well (mL), and t is the reaction time (minutes).

For calcium quantification, used as a late marker of osteogenesis, the samples were subjected to overnight digestion in 1 M HCl at 60°C (150 µL per sample) after 21 days of osteogenic differentiation. A standard curve for calcium detection was generated by serial dilutions of 1 M $CaCl_2$ in ultrapure water to produce 8-point triplicate standards (0–1000 ng $Ca^{2+}$ per well). Subsequently, 10 µL of either standards or diluted samples were mixed with 140 µL of a cresolphthalein-based working dye solution. After incubating the mixtures in the dark for 10 minutes at room temperature, the absorbance was recorded at 580 and 750 nm to measure the chromogenic purple complex formed between $Ca^{2+}$ and cresolphthalein, with background correction applied as needed (Multiskan SkyHigh Microplate Spectrophotometer, ThermoFisher Scientific).

To assess chondrogenic differentiation of the encapsulated MSCs, Alcian Blue staining was used to detect glycosaminoglycans (GAGs). After removing the supernatant, cultures were rinsed twice with DPBS and fixed in 4% PFA for 2 hours at room temperature. Following fixation, samples were stained with 150 µL of 1% (w/v) Alcian Blue in 0.1 M HCl for 4 hours. Excess dye was washed away with PBS (4 times). For quantitative analysis, Alcian Blue was extracted by incubating the samples with 150 µL of 6 M guanidine HCl for 2 hours on a plate shaker. The extracted dye (50 µL) was mixed with an equal volume of 6 M guanidine HCl and measured using a spectrophotometer at 650/750 nm (Multiskan SkyHigh Microplate Spectrophotometer, ThermoFisher Scientific). Absorbance values were used to quantify GAG content, with blank wells serving as controls for background correction.

To assess adipogenic differentiation, oil Red O staining was performed to detect lipid accumulation. Following removal of the medium, the cells were washed with DPBS and fixed with 4% PFA for 2 hours at room temperature (150 µL per well). After fixation, the wells were washed with ultrapure water. The cells were first incubated with 150 µL of 60% isopropanol per well for 5 minutes, followed by the addition of 150 µL of Oil Red O solution to each well for 15 minutes at room temperature with shaking. The Oil Red O solution was then removed, and the wells were briefly washed with 60% isopropanol for 30 seconds. To destain, 150 µL of 100% isopropanol was added to each well and incubated for 5 minutes with shaking. The resulting 100 µL of the destained solution was transferred to a new well, and absorbance was measured using a spectrophotometer at 510/750 nm. The corrected absorbance was calculated by subtracting the OD 750 nm reading from the OD 510 nm reading to quantify lipid accumulation in the cells.

## 2.8 Statistical analysis

Statistical analysis of the obtained data was conducted using Prism GraphPad Software version 10.2.2. The normality was assessed (using the Shapiro-Wilk test and by evaluating the Q-Q plots), and then a one-way or two-way ANOVA test with post-hoc multiple comparisons was applied to compare the different experimental groups. The selected tests are indicated in the captions of each figure. A p-value of less than 0.05 was considered statistically significant for differences between groups. The symbols representing the significantly different levels are indicated on the graphs, and/or defined in the captions (i.e. ns = $p > 0.05$; * = $p \leq 0.05$; ** = $p \leq 0.01$; *** = $p \leq 0.001$; **** = $p \leq 0.0001$).

# 3. Results and discussion

## 3.1 Material synthesis and characterization

### *3.1.1 Development of photo-crosslinkable gelatins and determination of degree of substitution*

The development of thiolated gelatin (GelSH) and gelatin-norbornene (GelNB) yielded biomaterials, each with functional groups optimized for photo-crosslinking.[13] GelSH was obtained through modification of gelatin with N-acetyl-homocysteine thiolactone to introduce thiol groups, while GelNB was obtained through gelatin functionalization with norbornene groups to enable rapid photo-crosslinking via thiol-ene chemistry under light exposure.[15,41] These modifications were carefully controlled to achieve specific degrees of substitution that allow tunable mechanical properties. The selection of GelSH and GelNB was motivated by their ability to undergo fast, efficient polymerization [42], which is critical for the precision and structural integrity required in volumetric additive manufacturing (VAM), especially for creating complex 3D hydrogel structures suitable for tissue engineering applications.[14,16,43]

An OPA assay was employed to assess the functionalization levels of thiolated gelatin as a function of the equivalents of N-acetyl homocysteine thiolactone (1eq, 3eq, and 5eq) and of norbornene-modified gelatin. The results indicated that the DS of GelSH5eq was the highest with 62.8 ± 2.3% followed by GelSH3eq being 53.8 ± 0.4% and lastly GelSH1eq with a DS of 38.9 ± 4.5%. For GelNB, only one variant was developed (with a targeted DS of 60%). The DS was determined both by the OPA assay and $^{1}$H-NMR spectroscopy (Figure S4). The OPA assay yielded a DS of 67.1 ± 4.6% whereas the latter yielded a lower DS of 55%. These results are in line with previously reported data on GelSH and GelNB (DS of 67-72% for GelSH5eq and DS of 53% via NMR spectroscopy for GelNB1.2eq) [30,41] and it can thus be concluded that the materials were successfully functionalized. Due to the overlap of the NMR signals of norbornene and N-acetyl-L-cysteine with the reference signal of gelatin (at 1 ppm), it is difficult to

accurately quantify the DS using $^{1}$H-NMR [44], which can also explain the differences in DS when comparing the results of $^{1}$H-NMR spectroscopy and the OPA assay. For further annotations in the manuscript, we refer to the developed materials (based on the DS determined via OPA) as GELSH39, GELSH54 and GELSH63, for the 1, 3 and 5 eq, respectively. Because only 1 variant of GELNB was developed (i.e. 1.2 eq), we will simply refer to it as GELNB.

### *3.1.2 In situ hydrogel crosslinking behavior via photorheology*

Photorheology was performed to investigate and compare the cross-linking behavior and the mechanical properties of the GelNB-GelSH hydrogels at varying concentrations (5, 7.5, and 10% (w/v)) and modification degrees (39%, 54% and 63%). The storage modulus (G'), which indicates the mechanical strength of the gels was evaluated. The values of G' can vary significantly based on the specific formulation and crosslinking conditions employed. In studies involving gelatin-based hydrogels, it has been observed that the storage modulus is influenced by the degree of substitution and the concentration of the gelatin precursors applied. For instance, it has been reported that increasing the degree of substitution in gelatin hydrogels leads to a higher storage modulus due to a denser and stiffer network structure.[41] Similarly, the mechanical properties of GelNB hydrogels can be tuned by adjusting the concentration of the thiol and norbornene components, which directly affects the crosslinking density and consequently the G' values.[45] Moreover, the rheological properties of GelNB-GelSH hydrogels have already been characterized in various studies. For example, the storage modulus of GelNB-based hydrogels has been reported to range from approximately 0.2 to 17 kPa depending on the crosslinking density and formulation.[21,35,46,47] This variability underscores the tunability of the mechanical properties of these hydrogels, which is essential for applications in tissue engineering and regenerative medicine.

Our results (Figure 5) clearly showed a trend where increasing the concentration of GelNB-GelSH resulted in a higher storage modulus. For example, GelNB-GelSH63 at 10% (w/v) exhibited the highest G' values (~12.5 kPa), significantly outperforming the GelNB-GelSH63 formulations at lower concentration, i.e. 5 and 7.5% (w/v). Similarly, a lower modification degree (e.g., GelNB-GelSH39) resulted in weaker gels, as demonstrated by consistently lower G' values compared to the GelNB-GelSH63 formulations. The significant differences in mechanical properties between the different formulations ($p < 0.01$) stress the importance of optimizing both the concentration and modification degree of the hydrogels for specific tissue engineering applications. Generally, stiffer hydrogels with higher G' values, mimicking the rigid environment of bone tissue, have been shown to promote osteogenic differentiation. More specifically, bone TE studies have reported G' values in the kPa to

MPa range, depending on the hydrogel composition and cell type.[21,48,49] Hydrogels with intermediate G' values, typically in the kPa range, are often more conducive to chondrogenesis.[50–52] This reflects the softer and more flexible nature of cartilage compared to bone. Softer hydrogels with lower G' values, typically in the < 2 kPa range, tend to favor adipogenesis.[41,53,54] This mimics the compliant environment of adipose tissue. Comparing these literature data to our findings (Figure 5), our GelNB-GelSH63 formulation at 10% (w/v) exhibited a G' of ~12.5 kPa, which is situated within the lower end of the range for osteogenesis, while the G' values of our other formulations, particularly at higher concentrations, align with the kPa range associated with chondrogenesis and adipogenesis.

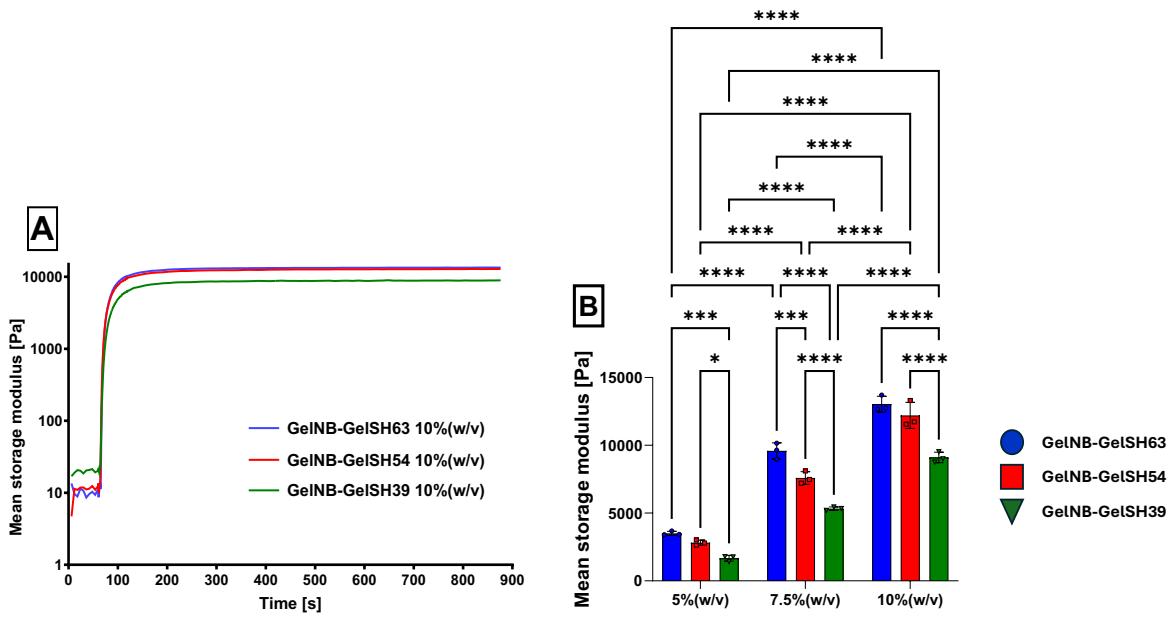


*Figure 5. (A) Photorheology comparison of GelNB-GelSH39, 54 and 63 (i.e. 1eq, 3eq and 5eq) for 10% (w/v), all with 0.006 w/v% photo-initiator. (B) Plateau values of storage moduli (G'), measured by photorheology, of GelNB-GelSH solutions (1 eq, 3eq and 5eq for 5, 7.5 and 10 w/v%). Data was analyzed using a two-way ANOVA and a Tukey's multiple comparisons test. (* = p ≤ 0.05; ** = p ≤ 0.01; *** = p ≤ 0.001; **** = p ≤ 0.0001)*

### *3.1.3 Determination of hydrogel gel fraction and mass swelling ratio*

In terms of gel fraction, gelatin-based hydrogels generally exhibit high gel fractions, often reported to be around 90% or higher.[21,41] Across all concentrations and combinations used in this work, the gel fraction is close to 100% (Figure 6). This indicates both proper crosslinking, as very few unmodified or uncrosslinked chains remain in the hydrogel as well as little to no leaching of potentially harmful compounds. With regard to cell viability, another important characteristic is the hydrogel's capacity to mimic the highly aqueous extra-cellular matrix (ECM) of tissues. To this end, the mass swelling ratio q was determined by evaluating the difference between the dried state and the swollen state of the gels. The mass swelling ratios ranged between 20 and 60 for 10% (w/v) to 5% (w/v) concentrations, being consistent with previously reported values for similar hydrogel systems.[15,21,30,35,41] The

swelling behavior of GelNB-GelSH hydrogels is attributed to the hydrophilic nature of gelatin and the crosslinked network structure, which allows for significant water uptake while maintaining structural integrity.[55] While these swelling ratios indicate the formation of robust hydrogels, their suitability for optimal cell response depends on the specific cell type and anticipated application.[56,57] The swelling ratio can be influenced by various factors, including the degree of crosslinking and the specific formulation of the hydrogel. For instance, hydrogels with higher crosslinking densities tend to exhibit lower swelling ratios due to the reduced mobility of polymer chains, which limits the amount of water that can be absorbed.[41,58] Generally, it can be observed that the mass swelling ratio decreases with an increasing concentration of the material. This highlights the complex interplay between DS, concentration, and network properties in GelNB-GelSH hydrogels.

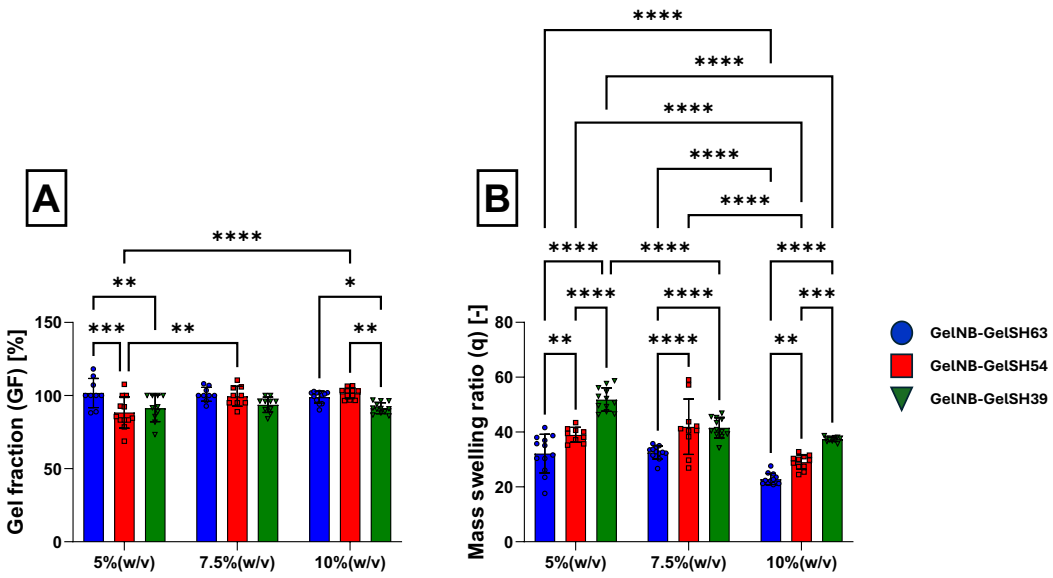


*Figure 3. Gel fraction (A) and mass swelling ratio (B) on the various gelatin solutions (GelSH with a DS of 63, 54 and 39, GelNB-GelSH concentrations of 10, 7.5 and 5% (w/v)). A two-way ANOVA and a Tukey's multiple comparisons test was selected. (* = p ≤ 0.05; ** = p ≤ 0.01; *** = p ≤ 0.001; **** = p ≤ 0.0001)*

### *3.1.4 Mechanical characterization of crosslinked GelNB-GelSH*

The mechanical characterization of GelNB-GelSH hydrogels through frequency sweep analysis and ring tensile testing provides valuable data on the hydrogels' viscoelastic properties and tensile strength. These properties can be correlated with the biophysical cues that influence MSC differentiation.[28,30,59] For example, the storage modulus obtained from frequency sweeps can indicate the stiffness of the hydrogel, a critical factor in determining the differentiation pathway of encapsulated MSCs. However, tensile testing is particularly important for assessing the hydrogel's ability to withstand macro-scale forces encountered *in vivo*, such as those associated with movement, muscle contraction, or blood flow.[34] Tensile testing provides information such as the ultimate

tensile strength, the elongation at break, and the Young's modulus, which are critical for predicting mechanical integrity and durability under physiological conditions.[60] These data can aid in determining whether the hydrogel will maintain its structure and support cellular activities, such as migration and adhesion, within a dynamic *in vivo* environment.

Given that the cells would be in a swollen equilibrium environment, mechanical properties were assessed via frequency sweep analysis (on equilibrium swollen hydrogel samples). The hydrogels were subjected to a constant 0.5N force under a rheometer spindle and underwent a frequency sweep. The mean storage and loss moduli (at 1 Hz) are presented in Figure S5. The compressive modulus E was calculated using Equation 6, assuming a Poisson's ratio of 0.5.[30] As observed previously, decreasing concentration and functionalization degree led to lower mechanical strength, albeit not statistically significant. This trend can be attributed to the decrease in crosslinking density. GelNB-GelSH63 at 10% (w/v) exhibited the highest E at 10.0 ± 2.4 kPa, while GelNB-GelSH54 at 5% (w/v) displayed the lowest E at 3.2 ± 2.2 kPa. By tailoring the mechanical properties of the hydrogel, we aim to guide MSCs towards specific cell lineages. Considering that E-moduli around 2 kPa favor adipogenic differentiation [31] and 11-30 kPa promote osteogenesis [30], our hydrogels span a range relevant for various lineages.[61, 62] The material with the highest E (GelNB-GelSH63 at 10% (w/v)) shows promise for osteogenic differentiation, while the lower E values (e.g., GelNB-GelSH54 at 5% (w/v)) may be more suitable for chondrogenic or even adipogenic differentiation. This suggests that by adjusting the hydrogel formulation, we can potentially cover the full range of mechanical properties required to guide differentiation towards osteogenic, chondrogenic, and adipogenic lineages. Furthermore, the concentration of the hydrogel can influence other important factors, including the printing resolution and the porosity. Higher concentrations may lead to improved printability but can also result in reduced porosity, potentially affecting cell-material interactions and nutrient and waste product diffusion. Optimizing the hydrogel concentration is essential for achieving the desired balance between mechanical properties and structural characteristics.

In addition to the frequency sweep analysis, tensile testing on ring-shaped samples was also conducted. Ring-shaped samples were used for tensile testing instead of dogbone-shaped samples to prevent failure at the grips, as gelatin-based hydrogels are prone to tearing under the harsh clamping conditions needed to prevent slippage. The ultimate tensile strength (UTS), the Young’s modulus (YM), and the maximum strain were determined (Figure 7). The UTS, which measures the maximum stress a material can withstand before failure, showed a consistent trend, increasing with the polymer concentration. The highest UTS was observed in GelNB-GelSH63 at 10% (w/v), with a value of 23.88 ±

4.78 kPa. Notably, there was no significant difference in UTS when comparing the 10% (w/v) formulations for GelNB-GelSH39, 54 and 63 substitutions (i.e. 1, 3 and 5 eq). Similarly, the YM, reflecting the stiffness of the hydrogels, increased with the polymer concentration. The GelNB-GelSH formulations at 5, 7.5 and 10% (w/v) exhibited Young's moduli of 0.6 ± 0.1, 0.7 ± 0.1, and 1.2 ± 0.2 kPa for the GelNB-GelSH63 variant, respectively. This is in agreement with a previous report from Yu *et al.* [61] who demonstrated that tensile moduli ranged between 0.5-5 kPa for GelNB-GelSH hydrogels with increasing concentrations between 5 and 15% (w/v) (molar ratio 1:1). No statistically significant difference in maximum strain was observed across the different formulations, despite the variations in UTS and YM. One potential explanation for this is that the crosslinking density, while impacting stiffness and strength, may have reached a plateau where further changes do not significantly affect the extensibility or strain at failure. Parmentier *et al.*[21] investigated this elastic behavior of gelatin hydrogels in detail and demonstrated that with increasing crosslinking densities of GelNB gels, no changes in elasticity could be observed. Additionally, the viscoelastic nature of the hydrogels might contribute to energy dissipation, resulting in similar strain values across formulations. It can thus be concluded that while higher concentrations and substitution degrees improve the mechanical strength and stiffness, the strain behavior remains consistent. As mechanical strength and stiffness are key factors for supporting osteogenic differentiation, which is rather difficult to reach with natural hydrogels, the GelNB-GelSH63 formulation at 10% (w/v) was selected for biofabrication using VAM and film casting.

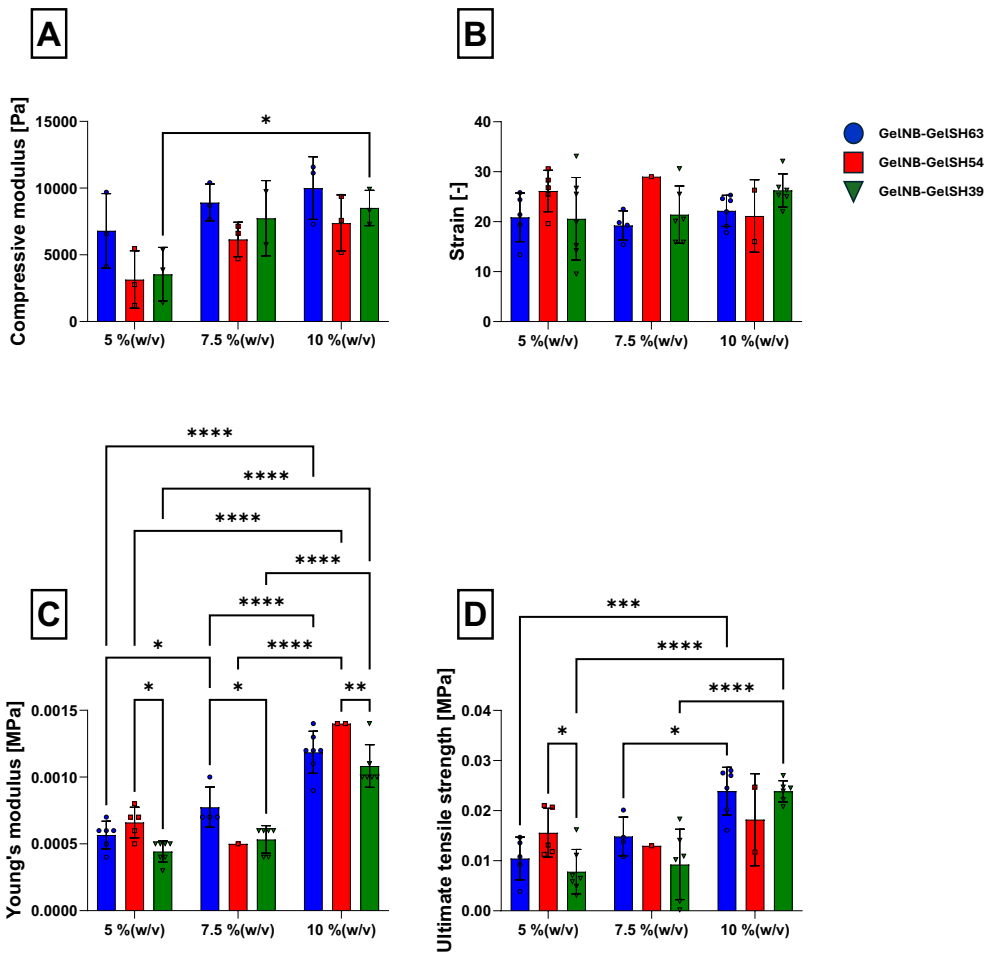


*Figure 4. Mechanical properties of the crosslinked gelatin-based hydrogels (at equilibrium swelling): Mean compressive modulus determined via frequency sweep analysis on equilibrium swollen crosslinked discs (A); Strain [-] (B); Young's modulus [MPa] (C) and Ultimate tensile strength [MPa] (D) determined via tensile testing on ring-shaped samples. A two-way ANOVA and a Tukey's multiple comparisons test was selected. (* = p ≤ 0.05; ** = p ≤ 0.01; *** = p ≤ 0.001; **** = p ≤ 0.0001)*

## 3.2 Volumetric printing of GelNB-GelSH

### *3.2.1 Resin development and characterization*

First, an acellular resin was developed to investigate the printability as well as the highest obtainable resolution of the GelNB-GelSH63 formulation. A higher% (w/v) of photoinitiator is needed in volumetric printing (as compared to the traditional film casting) because the entire 3D structure is cured simultaneously, requiring sufficient light absorption and uniform polymerization throughout the resin volume, even within complex scaffold geometries.[62–64] Based on reported values for similar hydrogel systems (0.05% (w/v) LAP for 5% (w/v) GelNB:4-arm-PEG-thiol [65], 0.05% (w/v) LAP for GelNB-GelSH [66] and 0.1-0.5% (w/v) LAP for 5% (w/v) GelMA [64,67]), and following optimization, a final concentration of 0.05% (w/v) LAP was selected for VAM printing in this work. Next, the absorbance and the refractive index of the resin at 405 nm were determined to be 0.3738 and 1.334,

respectively. Lastly, the optimal dose was determined by a combination of photorheology and the dose test. Using photorheology (Figure 8), a non-crosslinking interval of 5.5 seconds was observed, which allows sufficient light penetration without attaining the necessary dose for crosslinking, a crucial requirement for volumetric printing. In addition, the gel point, as obtained after plotting all data, was 6.2 seconds corresponding to a dose of 45 mJ·cm$^{-2}$ which was used as the initial reference dose. To further refine this result under conditions more representative of the volumetric printing process, a second dose test was conducted following the Readily3D dose test (Figure 8B). This test yielded an optimized dose of 56 mJ·cm$^{-2}$, reflecting differences in light distribution and exposure dynamics between photorheology and the volumetric setup.

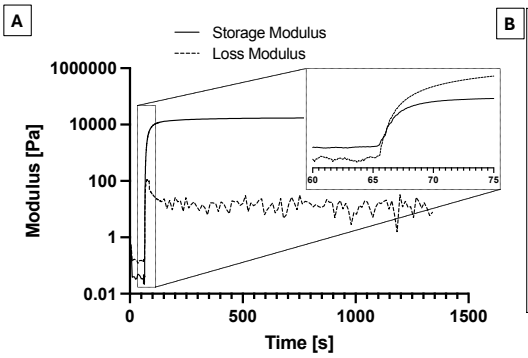


B

| Intensity [mW·cm$^{-2}$] | 5.83 | 7.12 | 8.69 | 10.62 | 12.96 |
|---|---|---|---|---|---|
| 6.48 | Small Dot | Large Dot | Large Dot | Large Dot | Large Dot |
| 5.31 | Small Dot | Large Dot | Large Dot | Large Dot | Large Dot |
| 4.35 | Barely Visible Dot | Large Dot | Large Dot | Large Dot | Large Dot |
| 3.56 | No Dot | Barely Visible Dot | Small Dot | Large Dot | Large Dot |
| 2.92 | No Dot | No Dot | Barely Visible Dot | Barely Visible Dot | Barely Visible Dot |
| | Time [s] | | | | |

*Figure 5. Determination of the reference dose for VAM printing. (A) Photo-rheology analysis to determine the gel point and required light dose for hydrogel crosslinking. The storage modulus (solid line) and loss modulus (dashed line) were monitored over time, with a gelation point observed at the crossover. The inset highlights the modulus increase during the gelation process. (B) Evaluation of reference doses using the Readily3D protocol, showing the relationship between light intensity (mW·cm$^{-2}$) and exposure time (s) to achieve effective crosslinking."*

### *3.2.2 Post-processing curing*

In a next part of the work, we evaluated the curing efficiency of gelatin hydrogels comparing 405 nm with UV-A (320-380 nm) irradiation. The choice of wavelength is critical, especially for applications involving cell encapsulation, where minimizing cytotoxicity is essential. Light at a wavelength of 405 nm is generally preferred for its lower cytotoxicity, while UV-A offers more rapid curing.[68,69] Our focus was on determining the crosslinking efficiency through HR-MAS NMR spectroscopy while keeping irradiation times as short as possible to ensure high cell viability. The results (Figure S6) showed no significant differences in double bond conversion between the two light sources nor across the different curing times (5, 10, and 15 minutes). Without post-processing curing, the double bond conversion was 60%. After post-processing curing, high conversion rates (above 90%) were observed at all time points, demonstrating that the post-processing process was rapid and effective in achieving complete crosslinking. The absence of significant variation between the two light sources suggests

that both UVA and 405 nm wavelengths are equally effective in promoting hydrogel formation. Therefore, either can be used for post-curing without compromising crosslinking quality. Importantly, 405 nm was identified as a preferable light source for crosslinking due to its reduced negative impact on cells [70,71], while still achieving a high double bond conversion, even at shorter irradiation times (96.2% at 5 minutes).

## 3.3 VAM-printed scaffold characterization

### *3.3.1 CAD/CAM mimicry*

The CAD/CAM mimicry achieved through volumetric printing is shown in Figure 9. The left panel presents an IWP structure with a lattice configuration and interconnected pores. The CAD model captures the porous architecture and overall cylindrical shape, which is faithfully reproduced in the printed scaffold. This highlights the capability of the VAM system to accurately and quickly translate complex 3D geometries into physical structures with high precision. The IWP design (Figure 9.C), characterized by its repeating porous architecture, serves as an example of how VAM can produce intricate, scaffold-like structures suitable for biomedical applications. The right panel showcases a more intricate benchmark CAD design, featuring circular holes, pillars, steps, crosses, and thin walls. The smallest observed features include holes and pillars at 340 µm, steps at 210 µm, and crosses and walls at 120 µm, as shown in the red markers on the CAD design (Figure S7). In comparison, values found in literature for gelatin polymer solutions include a positive resolution of 138.83 ± 52.47 µm and negative resolution of 198.97 ± 51.84 µm for GelNBNB+GelSH containing 0.025% (w/v) LAP [6], a negative resolution of ± 380 µm for GelNB+4-arm thiolated poly(ethylene glycol) containing 0.075% (w/v)% LAP [10], a positive resolution of 244 ± 16 µm and a negative resolution of 461 ± 26 µm for GelMA with 5% (w/v) LAP [72], as well as 23.68 ± 10.75 µm for GelNB+dithiothreitol/diethylene glycol with 0.1% (w/v) LAP [73]. The photographic image (Figure 9.B) confirms the successful replication of these intricate details, with the VAM-printed structure retaining 109.01% of the original CAD dimensions after equilibrium swelling. Further evaluation using optical microscopy and SEM imaging (Figure S7 and S8) reveals that, although some challenges such as slight rounding of edges and difficulties in printing positive features were encountered, the majority of the features were accurately reproduced. SEM images of the printed benchmark (Figure S9) show walls with a thickness of 85 µm, closely matching the CAD design. This combination of optical and SEM imaging confirms the high fidelity of VAM printing in replicating complex CAD designs, with only minor deviations in the smallest, most intricate features.

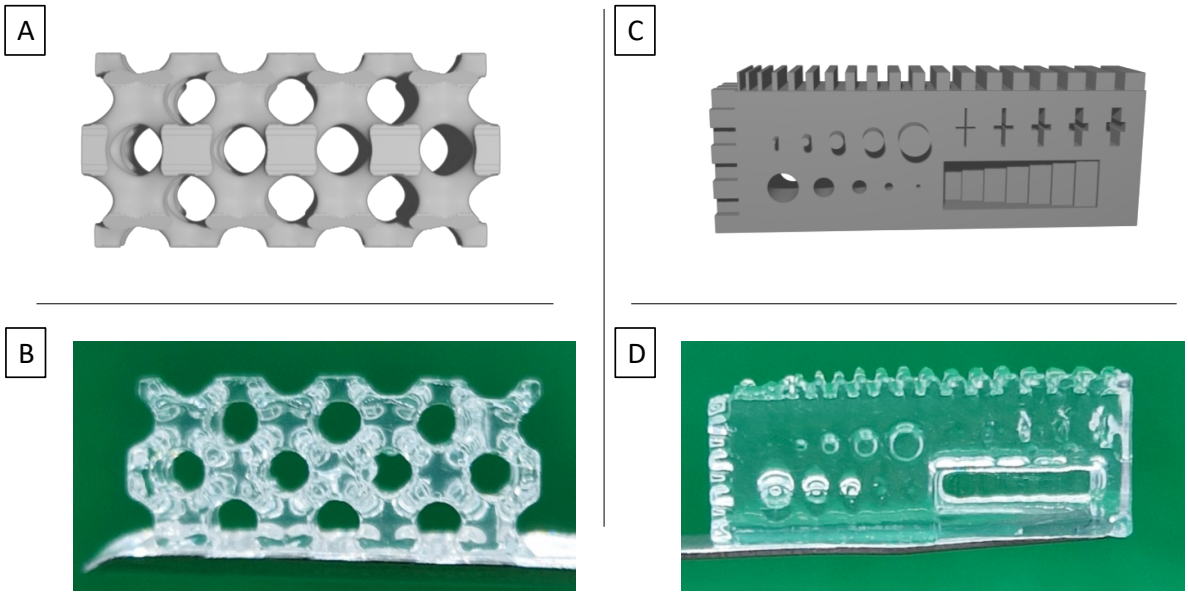


*Figure 6. CAD/CAM mimicry of VAM-printed structures: (A) 3D image of the IWP design (CAD) and (B) the VAM-printed IWP design (CAM); (C) 3D image of the benchmark (CAD) and (D) the VAM-printed benchmark (CAM).*

### *3.3.2 Mechanical characterization*

The mechanical properties of VAM-printed hydrogel cubes composed of GelNB-GelSH63 at 10% (w/v) were evaluated through compression testing and oscillatory rheology, as outlined in section 2.6.2. After swelling, the cubes measured approximately 5.25, 5.25, 5.12 mm in length, width and height, respectively. The mechanical tests showed consistent behavior across the triplicate samples (Figure 10). The hydrogels initially exhibited a linear elastic response, where the force increased proportionally with the displacement. However, at higher forces, the elasticity became non-linear. As compression continued, the hydrogels eventually reached a critical stress point, leading to structural collapse. The hydrogels demonstrated a maximum strain of 69.7% and withstood a considerable compressive force before failure, with an average compressive strength of 507.63 ± 53.15 kPa.

VAM-printed GelNB-GelSH63 discs, with a diameter of 8.8 mm and a height of 1.5 mm after equilibrium swelling, were evaluated using oscillatory rheology. The analysis revealed that these hydrogel scaffolds exhibited a storage modulus of 7.014 ± 0.715 kPa and a loss modulus of 0.077 ± 0.007 kPa, reflecting their viscoelastic nature. This corresponds to a compressive modulus (E) of 21.04 ± 2.14 kPa. To compare, frequency sweep analysis of film casted GelNB-GelSH63 samples (at 10% (w/v)) indicated a storage modulus of 2.156 ± 0.515 kPa, corresponding to an E modulus of 6.467 ± 0.154 kPa. This value is approximately 3.5 times lower than that of the VAM-printed scaffolds, suggesting significant differences in their mechanical properties. These differences can be attributed to variations in double bond conversion and as a result the mechanical properties, as demonstrated by HR-MAS (95.0% for VAM-printed *versus* 41.7% film casted, Figure S10). This increased conversion

is largely due to differences in processing methods. Specifically, the post-processing curing step in VAM printing enhanced double bond conversion from 60.6% to 95.0% (see section 3.2.2), whereas the cell encapsulation protocol for film-casted constructs involved 10 minutes of physical crosslinking followed by 10 minutes of UV irradiation, with a lower PI concentration.[30,41]

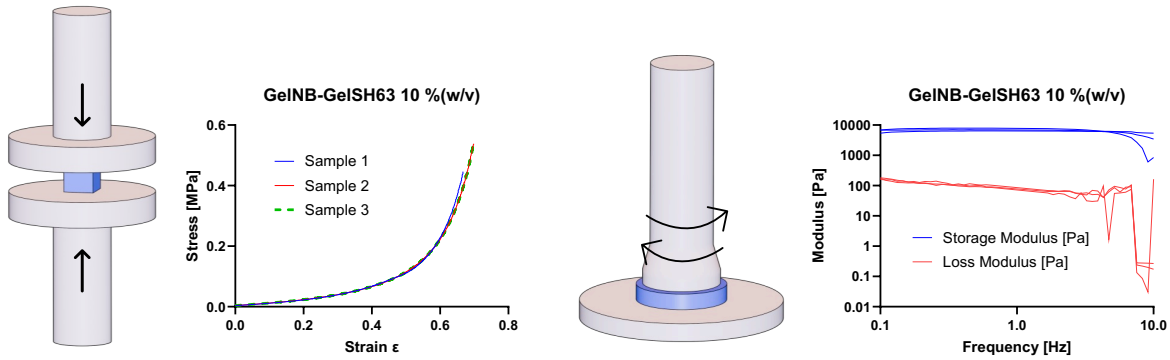


*Figure 7. Compression testing and frequency sweep analysis on VAM-printed cubes and discs, respectively.*

## 3.4 Optimization of the bioresin for volumetric bioprinting

In the previous section, an acellular resin was prepared, volumetrically printed and characterized. However, to achieve the goal of encapsulating cells within the final scaffolds, further optimization steps were necessary. The inclusion of cells introduced light scattering effects, which can lead to print defects and reduced resolution. Additionally, the presence of cells affected the photopolymerization dynamics, prompting us to reassess and refine the photorheology to ensure consistent crosslinking and scaffold fidelity. An important aspect when performing VAM with cells is to tune the refractive index (RI) of the resin to that of the cell cytoplasm to avoid undesired scattering and print defects. The cytoplasm typically has a RI between 1.36 and 1.39, depending on the cell type.[75–78] Tuning of the RI can be achieved via addition of iodixanol, a cell-compatible, radio-opaque contrast agent with a refractive index of 1.429 (at 60% (w/v), commercially available as OptiPrep™).[77,79,80] Maintaining an iodixanol concentration as low as possible is essential as iodixanol has also been shown to impact the ductility and overall mechanical performance of scaffolds.[62,67,81] In brief, resins were supplemented with 0, 10, 15 or 20% (v/v) OptiPrep as well as MSCs at a concentration of $2{\cdot}10^{6}{\cdot}mL^{-1}$ while retaining a concentration of 10% (w/v) GelNB-GelSH63 and 0.05% (w/v) LAP. The lowest RI within the range for the cytoplasm was found using 15% (v/v), being 1.3623 (other RI can be found in Figure S11 and Table S2). Next, the absorbance at 405 nm of the complete bioresin indicated 0.587. Lastly, the gel point was determined using photorheology (Figure S12) and used as the initial reference dose, 36 $mJ{\cdot}cm^{-2}$, for the second dose test (Figure 11). The second dose test was then performed using the Readily3D protocol for VAM printing, yielding an optimized dose of 71 $mJ{\cdot}cm^{-2}$.

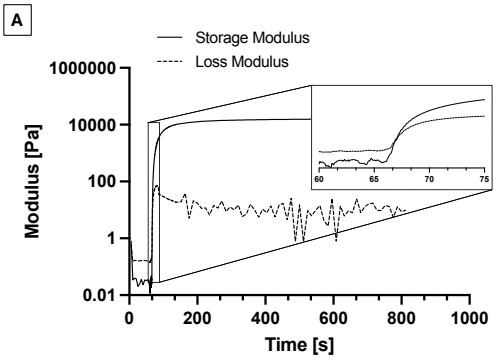


B

| Intensity [mW·cm$^{-2}$] | 5.83 | 7.76 | 10.32 | 13.73 | 18.26 |
|---|---|---|---|---|---|
| 9.13 | No Dot | Large Dot | Large Dot | Large Dot | Large Dot |
| 6.86 | No Dot | Small Dot | Large Dot | Large Dot | Large Dot |
| 5.16 | No Dot | Barely Visible Dot | Large Dot | Large Dot | Large Dot |
| 3.88 | No Dot | No Dot | Barely Visible Dot | Large Dot | Large Dot |
| 2.92 | No Dot | No Dot | No Dot | Barely Visible Dot | Small Dot |
| | Time [s] | | | | |

*Figure 8. Determination of the reference dose for VAM printing. (A) Photo-rheology analysis to determine the gel point and required light dose for hydrogel crosslinking. The storage modulus (solid line) and loss modulus (dashed line) were monitored over time, with a gelation point observed at the crossover. The inset highlights the modulus increase during the gelation process. (B) Evaluation of reference doses using the Readily3D protocol, showing the relationship between light intensity (mW·cm$^{-2}$) and exposure time (s) to achieve effective crosslinking.*

## 3.5 Biological characterization of encapsulated MSCs

Recently, interest has grown in understanding how different microenvironments, such as those provided by hydrogels, influence the behavior of MSCs, particularly when comparing film casted cells versus printed cells.[82–84] This study aimed to evaluate the biological properties, specifically proliferation and tri-lineage differentiation, of MSCs processed using two methods: biofabrication using VAM printing and encapsulation via film casting. By assessing these differences, we sought to determine how the structural variations introduced by these techniques impact cell behavior.

### *3.5.1 Viability and proliferation assay*

The MTS assay results, normalized to Day 0 film casted samples, provide valuable insights into the proliferation of encapsulated MSCs during 21 days of culture. Both groups, VAM-printed versus film casted, exhibited significant increases in absorbance, indicating successful proliferation (Figure 12), with a notable interaction between both the processing method and time points of the measured outcomes ($p < 0.0001$). On day 0, there was a significant difference between VAM-printed and film casted samples ($p = 0.0027$), with film casted samples showing higher absorbance values. This can be attributed to the slightly longer preparation protocol of the VAM printing process, which may have led to an initial delay in cell proliferation. By day 7, no significant difference was observed anymore between both methods ($p = 0.9054$). This suggests that the MSCs in the VAM-printed samples recovered and adapted to their environment, exhibiting a proliferation comparable with the film casted samples. This is in line with other studies, where encapsulated cells needed a few days to adjust to the new environment.[85]

At days 14 and 21, significant differences re-emerged ($p < 0.0001$ for both time points). While for both groups, cells continued to proliferate, the film casted samples exhibited a higher relative increase in cell number. This observation aligns with a growing body of literature highlighting the influence of hydrogel stiffness on cell behavior, particularly cell proliferation and - differentiation. For example, Tan *et al.* [49] demonstrated a correlation between hydrogel stiffness and cell fate, with softer materials tending to favor proliferation. Studies by Engler *et al.* [86] showed that matrix elasticity directed stem cell lineage specification, with softer substrates maintaining stemness and promoting proliferation. In our study, the film casted samples, being less crosslinked and having a lower E-modulus than the VAM-printed ones (as discussed in section 3.3.2), provide a more compliant and potentially more porous environment facilitating cell expansion and nutrient and waste product exchange.

However, it should be emphasized that the VAM-printed samples, despite their higher crosslinking density, still supported significant and sustained cell proliferation throughout the entire 21-day culture period, as evidenced by significant differences in absorbance between day 0 and later time points (D14 and D21, both $p < 0.0001$), and between day 7 and subsequent days (D14: $p = 0.0003$, D21: $p = 0.0059$). This is consistent with several studies demonstrating that cells can proliferate within even relatively stiff 3D-printed hydrogel constructs.[85,87] This finding highlights the versatility of VAM printing for creating scaffolds that can support cell viability and proliferation while also offering precise control over scaffold architecture. In the film casted group, significant increases were similarly evident from day 0 to day 14 and day 21 (both $p < 0.0001$), and between day 7 and the later time points (both $p < 0.0001$).

Moreover, the increased stiffness of the VAM-printed constructs (see mechanical characterization in section 3.2.2), may offer advantages in terms of directing cell differentiation towards specific lineages, such as osteogenic pathways, as suggested in literature.[49,86,88] This potential for modulating cell fate through scaffold stiffness, underscores the importance of considering the interplay between material properties and cellular responses in designing scaffolds for tissue engineering applications.

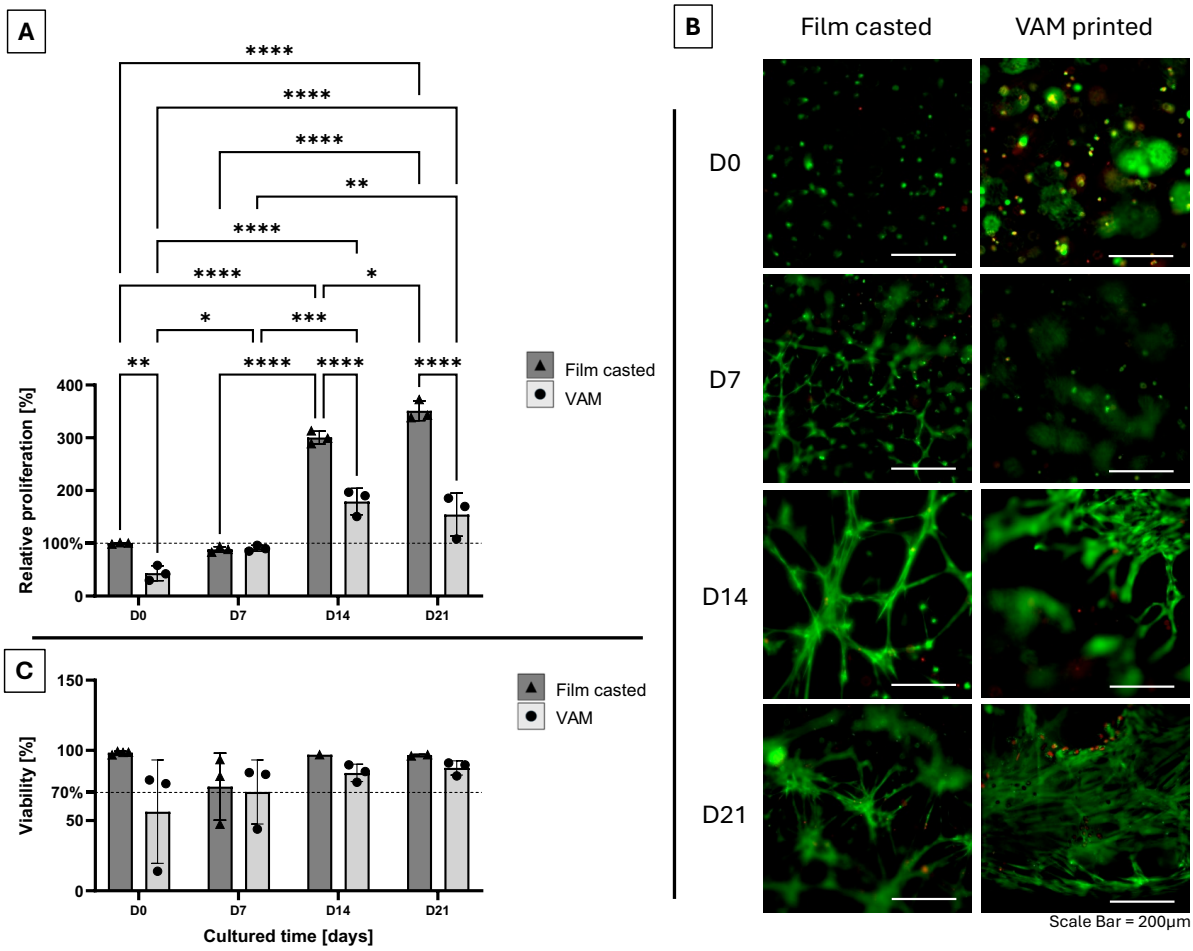


*Figure 9. (A) Evaluation of proliferation (through an MTS assay) of MSC in VAM-printed versus film casted encapsulation in GelNB-GelSH63 hydrogel (10% (w/v)) at different time points (day 0, 7, 14 and 21). The data was normalized against the D0 of the film casted group and analyzed using a two-way ANOVA with Sidak's multiple comparisons test. (* = p ≤ 0.05; ** = p ≤ 0.01; *** = p ≤ 0.001; **** = p ≤ 0.0001); (B) Viability (live/dead ratio) of both groups at the different time points; (C) Live/Dead (L/D) staining images of VAM-printed and film casted MSCs at different time points. Green indicates living cells, and red indicates dead cells. Scale bar: 200 µm.*

The live/dead (L/D) staining images (Figure 12, right) provide further insights into cell morphology within the hydrogel constructs. Cells near the surface (in both VAM and film casted samples) exhibited increased elongation over time, while those encapsulated deeper within the hydrogel maintained round. Despite these morphological differences, the MTS assay indicates that both populations remained viable and proliferative, suggesting that the microenvironment supports cell growth regardless of spatial positioning within the hydrogel. As a proof-of-concept to show the feasibility of printing porous scaffolds, the IWP design was volumetrically printed and the L/D was evaluated at day 3. Figure 13 shows the VAM-printed scaffold with mainly green-stained cells (living), as well as the difference in MSC morphology at the surface (elongated) and in the center (round-shaped) of the hydrogel.

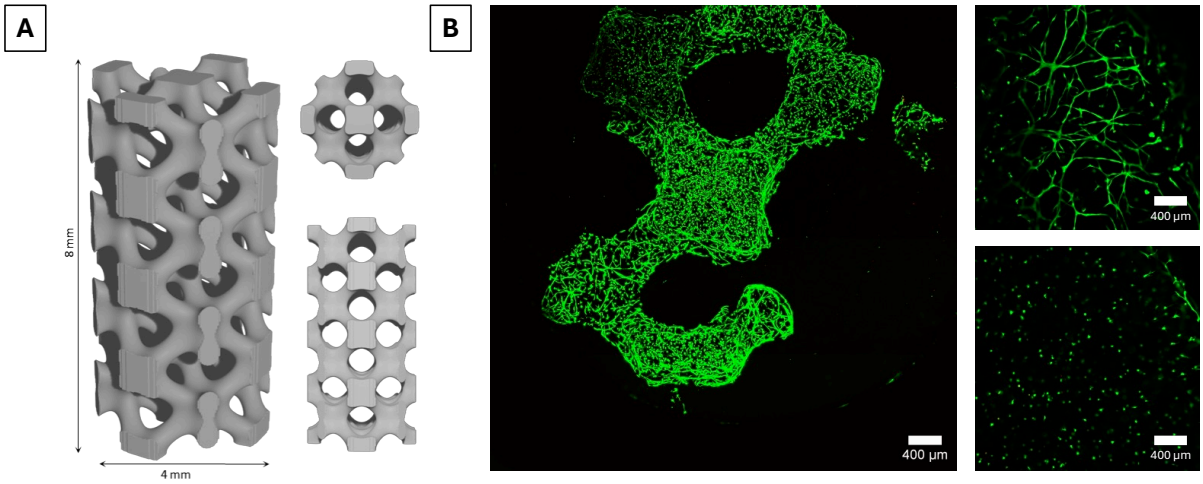


*Figure 10. (A) CAD image of the IWP structure; (B) Live/Dead (L/D) staining images of VAM-printed MSCs at day 3. Green indicates living cells, and red indicates dead cells. Scale bar: 400 µm.*

### *3.5.2 Differentiation assays*

Osteogenic differentiation was evaluated using alkaline phosphatase activity (ALP) and calcium deposition, and compared between VAM-printed and film casted hydrogels (Figure 14). Additionally, to evaluate the need of providing extra growth factors to support differentiation, the cell response to differentiation (DIFF) and normal expansion (CTRL) medium was compared. Notably, the VAM-printed DIFF group displayed a significant increase in ALP activity at day 7 compared to their film casted counterparts (vs CTRL: $p = 0.0350$, vs DIFF: $p = 0.0038$) indicating that VAM-printed scaffolds more effectively support early osteogenesis. This trend continued, with the VAM-printed scaffolds exhibiting markedly higher ALP activity after being cultured in DIFF medium for 21 days ($p < 0.0001$), suggesting an accelerated differentiation process within these constructs. An increase in ALP activity on stiffer gels has also been described by Mullen *et al.* [89]. Another study reported on significant changes in ALP activity with varying stiffness of the developed materials, with or without differentiation medium.[90]

Analogously, calcium production on day 21 revealed significantly elevated levels in the differentiated VAM-printed group compared to the film casted groups ($p < 0.0001$). The differentiated VAM-printed scaffolds showed the highest calcium deposition, indicative of enhanced late-stage osteogenesis. The sustained elevation in ALP activity alongside increased calcium levels in the VAM-printed scaffolds highlights the positive effect of VAM printing on osteogenesis. These findings suggest that the VAM-printed scaffolds create a more supportive environment for osteogenic differentiation, likely attributed to their more densely crosslinked network. It should also be noted that for both osteogenic differentiation assays, there is a significant increase in differentiation for the differentiated groups (DIFF) compared to the control groups (CTRL). This implies that osteogenic differentiation factors are

required to induce differentiation, and that there is a synergistic effect between the differentiation medium and the processing method (VAM printing) in terms of osteogenic induction. The latter has also been described by Tan *et al.* [49] who showed that the interactions of chemical and physical factors may work synergistically to enhance bone regeneration. Other synergistic effects that have been described regarding osteogenic differentiation include among other surface chemistry and surface topography [91], cell-derived extracellular matrices and topography [92], stiffness and structure of 3D-printed hydrogels [88], hydrogel stiffness and co-culture systems [64], surface topography and induction media [93].

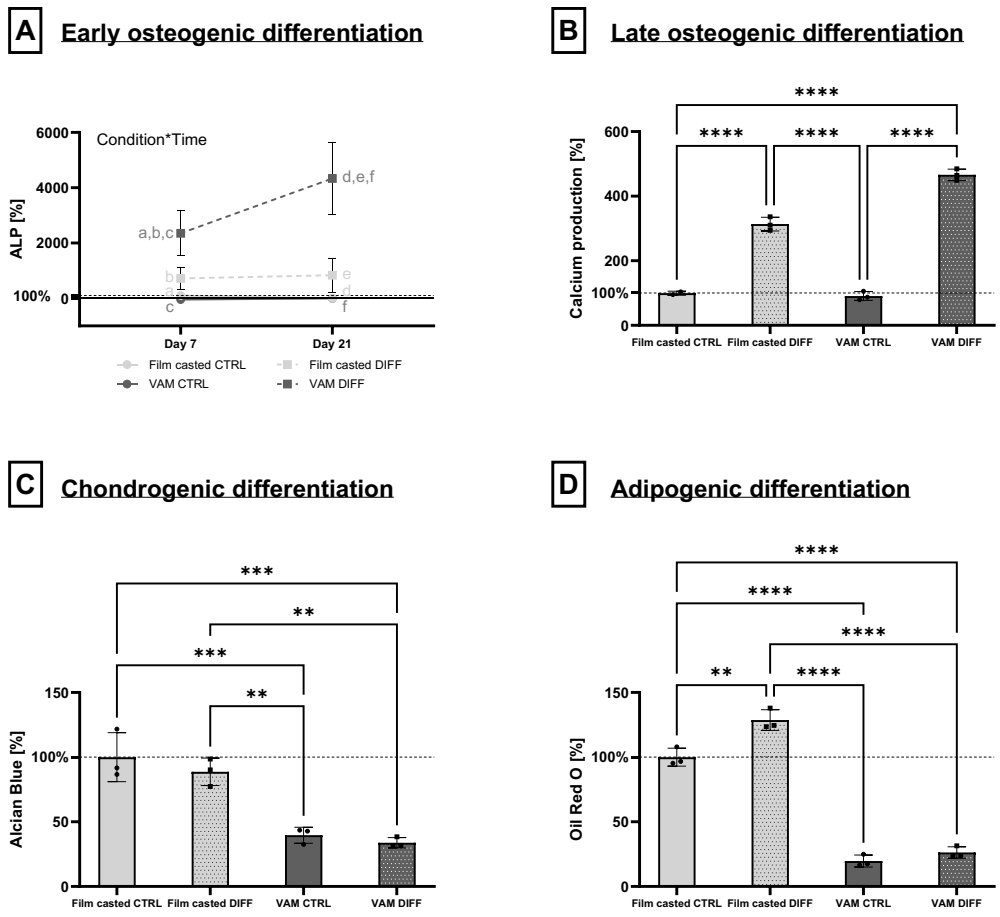


*Figure 11. Results of osteogenic (ALP activity (A) and Ca deposition (B)), chondrogenic (Alcian Blue, (C)) and adipogenic (Oil Red O, (D)) differentiation of MSCs encapsulated in VAM-printed vs film casted scaffolds (cultured in expansion (CTRL) or differentiation (DIFF) medium). The data was analyzed using a two-way ANOVA (ALP) or one-way ANOVA (Ca, Alcian Blue and Oil Red O) and a Tukey's multiple comparisons test. In (A), the letters 'a' to 'f' indicate the significant differences of the two-way ANOVA test between the groups that share the same letter: a: **, b and c: *, d, e and f: ****. (* = p ≤ 0.05; ** = p ≤ 0.01; *** = p ≤ 0.001; **** = p ≤ 0.0001)*

Chondrogenic differentiation was evaluated using the Alcian Blue staining to assess the presence of GAGs.[94–96] When comparing chondrogenic potential in the differentiated versus control samples, no significant difference in GAG production could be observed – though positive responses indicated

the presence of GAGs in both groups. This can be explained by the fact that the hydrogel scaffold might induce the chondrogenic differentiation of MSCs, irrespective of the used medium. It must also be mentioned that spontaneous chondrogenic differentiation of equine MSCs has been reported before [97,98], and was hypothesized to be linked to high-density culture conditions and hypoxia in the 3D cell culture system. This spontaneous chondrogenic differentiation potential has also been observed in human [99,100] and bovine MSCs [101,102]. Nevertheless, this assay further emphasizes the differences in GAG production between VAM-printed and film casted scaffolds. The GAG production in the VAM-printed groups significantly decreased ($p < 0.05$) compared to the film casted group. In a study by Goldshmid *et al.* [103] it was shown that chondrogenesis was favored in materials with a higher modulus (i.e. G' = 1000 Pa). It should be noted that in this study, different concentrations of PEG-diacrylate were used to modify the stiffness of a bovine PEG-fibrinogen hydrogel, meaning both mechanical and chemical properties could have influenced the observed chondrogenic response. Similarly, Zhou *et al.* [51] investigated the chondrogenic differentiation of MSCs using polyacrylamide-based hydrogels of varying stiffness (ranging from ~0.5 kPa to stiffer formulations), prepared by altering the acrylamide-to-bis-acrylamide ratio. They showed that the chondrogenic differentiation of MSCs is promoted by soft substrates (about 0.5 kPa). Since these studies compared different hydrogel compositions rather than a single composition with varying mechanical properties (as in our study), the observed effects on chondrogenesis could possibly be attributed to mechanical as well as chemical differences. In addition, further analysis indicated that TGF-β3 supplementation increased the expression level of cartilage-related markers and masked the stiffness-derived expression pattern of hypertrophic markers.[51]

Adipogenic differentiation of MSCs was assessed using the Oil Red O staining, which quantifies the lipid droplets intracellularly.[104–106] A robust lipid accumulation was observed in the film casted scaffolds cultured in differentiation medium (DIFF), indicating successful adipogenesis. The results revealed again distinct outcomes between VAM-printed and film casted scaffolds. In general, less adipogenic differentiation was observed in the VAM-printed group ($p < 0.0001$) as compared to the film casted group, regardless of the media used. In a study by Zhao *et al.* [107], where hydrogels with varying stiffness have been evaluated (from 0.15 to 4 kPa) using Oil Red O staining, the MSCs exhibited a smaller spreading area with much more stretched morphology on the 4 kPa hydrogels than on the hydrogels with lower stiffness. The finding that substrate elasticity plays a crucial role in directing stem cell differentiation towards specific lineages also applies to adipogenic differentiation.[108] For instance, soft substrates (E = 2 kPa) promote adipogenic differentiation [31], whereas stiff substrates (E = 34 kPa) favor osteogenic differentiation [86]. Wen *et al.* [109] identified substrate elasticity as the

primary factor influencing cell differentiation under unstrained culture conditions. In our study, the VAM-printed scaffolds showed an E of 21.04 ± 2.14 kPa (section 3.3.2) which is a 10-fold higher than the soft substrates of 2 kPa that promote adipogenic differentiation as described by Murphy *et al.* [31], which clearly explains the lower adipogenic differentiation results observed in the VAM-printed scaffolds.

The link between the mechanical properties of the VAM-printed scaffolds and their ability to support cell differentiation is pivotal in understanding these results.[110] As described in the section on the mechanical characterization of the VAM-printed scaffolds (section 3.3.2), a more efficient and denser crosslinking led to an E modulus of 21.04 ± 2.14 kPa that was 3-4 times higher than the film casted (E = 6.467 ± 0.154 kPa). This resulted in the increased osteogenesis observed in the VAM-printed scaffolds, while the lesser crosslinked film casted constructs supported the adipogenic and chondrogenic potential of encapsulated MSCs. It should also be mentioned that it is never one factor alone that is influencing MSC differentiation, but a combination of factors, e.g. substrate stiffness and surface topography [111], physico-mechanical and biomolecular cues [112], effect of matrix stiffness combined with TGF-β [108] or protein tethering [109].

In summary, we illustrated distinct differentiation outcomes for MSCs cultured in VAM-printed versus film casted constructs. The VAM-printed scaffolds exhibited significantly higher ALP activity and calcium deposition, confirming effective osteogenesis. Conversely, chondrogenic and adipogenic differentiation, assessed through Alcian Blue and Oil Red O staining, were more pronounced in the film casted groups. The inherent differences in crosslinking density and mechanical properties between VAM-printed and film casted scaffolds are significant. While not demonstrated in this study, it is possible to obtain softer gels through VAM by modifying the chemical composition, such as the degree of substitution of the modified gelatins or the gelatin concentration of the bioresin. Additionally, film casting with alternative protocols, such as extended irradiation or post-curing, could be used to yield stiffer constructs, potentially targeting osteogenic applications. However, when comparing both techniques regarding their potential to fabricate 3D scaffolds, only VAM printing enabled the creation of complex structures, offering greater design flexibility. This study lays the foundation for future research on optimizing material formulation within the VAM printing framework to enhance differentiation across multiple lineages, related to the specific tissue engineering applications.

# 4. Conclusions

This study highlights the potential of photo-crosslinkable gelatin hydrogels (GelSH and GelNB) for volumetric additive manufacturing, with a focus on their ability to guide MSC fate and differentiation for tissue engineering applications. Material characterization revealed a clear relationship between the degree of substitution and the mechanical properties: GelSH functionalized with 1, 3, and 5 equivalents exhibited DS values of 39%, 54%, and 63%, respectively, while increasing the hydrogel concentration from 5 to 10% (w/v) led to a corresponding increase in the storage modulus (G'). This tunable behavior, with G' ranging from 206 Pa to 12.5 kPa, highlights the versatility of these hydrogels in replicating diverse tissue environments.

When applied in VAM-printed constructs using GelNB-GelSH63 at 10% (w/v), the scaffolds demonstrated enhanced mechanical performance, with compressive strength reaching 507.63 ± 53.15 kPa and a compressive modulus of 21.04 ± 2.14 kPa. This structural integrity translated into significant biological benefits. VAM-printed scaffolds supported significant and sustained cell proliferation throughout the entire 21-day culture period. The more densely crosslinked network provided by the VAM-printed hydrogels also promoted osteogenic differentiation, as indicated by elevated ALP activity and calcium deposition when differentiation medium is used. In contrast, film casted hydrogels, with their softer and less dense crosslinked structure, favored chondrogenic and adipogenic differentiation. These findings underscore the critical role of scaffold physico-chemical properties in guiding cell behavior, demonstrating the potential of VAM to create customized hydrogel scaffolds for targeted tissue engineering applications.

# 5. Acknowledgement and funding

N. Pien, B. Bogaert and M. Meeremans would like to acknowledge the financial support of the Research Foundation Flanders (FWO) under the form of an FWO junior post-doctoral research grant (12E4523N), and FWO SB PhD fellowships (1SHE724N and 1S02822N), respectively. S. Van Vlierberghe acknowledges Interreg Healthy Teeth and the Research Foundation Flanders for providing a Hercules grant (I003922N).

# 6. References

[1] J. Groll, T. Boland, T. Blunk, J.A. Burdick, D.W. Cho, P.D. Dalton, B. Derby, G. Forgacs, Q. Li, V.A. Mironov, L. Moroni, M. Nakamura, W. Shu, S. Takeuchi, G. Vozzi, T.B.F. Woodfield, T. Xu, J.J. Yoo, J. Malda, Biofabrication: Reappraising the definition of an

evolving field, Biofabrication 8 (2016). https://doi.org/10.1088/1758-5090/8/1/013001.

[2] W.S. Harley, C.C. Li, J. Toombs, C.D. O'Connell, H.K. Taylor, D.E. Heath, D.J. Collins, Advances in biofabrication techniques towards functional bioprinted heterogeneous engineered tissues: A comprehensive review, Bioprinting 23 (2021). https://doi.org/10.1016/j.bprint.2021.e00147.

[3] S. Verma, V. Khanna, S. Kumar, S. Kumar, The Art of Building Living Tissues: Exploring the Frontiers of Biofabrication with 3D Bioprinting, ACS Omega 8 (2023). https://doi.org/10.1021/acsomega.3c02600.

[4] D. Loterie, P. Delrot, C. Moser, High-resolution tomographic volumetric additive manufacturing, Nat Commun 11 (2020). https://doi.org/10.1038/s41467-020-14630-4.

[5] I. Bhattacharya, J. Toombs, H. Taylor, High fidelity volumetric additive manufacturing, Addit Manuf 47 (2021). https://doi.org/10.1016/j.addma.2021.102299.

[6] J. Duquesne, L. Parmentier, E. Vermeersch, F. Lemaire, J. Won Seo, R.I. Dmitriev, S. Van Vlierberghe, Volumetric bioprinting of the osteoid niche, Biofabrication (2025). https://doi.org/10.1088/1758-5090/adab25.

[7] Q. Thijssen, A. Quaak, J. Toombs, E. De Vlieghere, L. Parmentier, H. Taylor, S. Van Vlierberghe, Volumetric Printing of Thiol-Ene Photo-Cross-Linkable Poly(ε-caprolactone): A Tunable Material Platform Serving Biomedical Applications, Advanced Materials 35 (2023). https://doi.org/10.1002/adma.202210136.

[8] Q. Thijssen, A.J. Ortega, R.P. Vieira, S. Van Vlierberghe, Radical inhibition in tomographic volumetric 3D printing for thiol-ene photoresists: From photorheology to printability, React Funct Polym 205 (2024) 106096. https://doi.org/10.1016/j.reactfunctpolym.2024.106096.

[9] J. Madrid-Wolff, A. Boniface, D. Loterie, P. Delrot, C. Moser, Controlling Light in Scattering Materials for Volumetric Additive Manufacturing, Advanced Science 9 (2022). https://doi.org/10.1002/advs.202105144.

[10] R. Rizzo, D. Rütsche, H. Liu, P. Chansoria, A. Wang, A. Hasenauer, M. Zenobi-Wong, Multiscale Hybrid Fabrication: Volumetric Printing Meets Two-Photon Ablation, Adv Mater Technol 8 (2023). https://doi.org/10.1002/admt.202201871.

[11] R. Levato, K.S. Lim, Harnessing light in biofabrication, Biofabrication 15 (2023). https://doi.org/10.1088/1758-5090/acb50f.

[12] J. Malda, J. Visser, F.P. Melchels, T. Jüngst, W.E. Hennink, W.J.A. Dhert, J. Groll, D.W. Hutmacher, 25th anniversary article: Engineering hydrogels for biofabrication, Advanced Materials 25 (2013) 5011–5028. https://doi.org/10.1002/adma.201302042.

[13] J. Van Hoorick, L. Tytgat, A. Dobos, H. Ottevaere, J. Van Erps, H. Thienpont, A. Ovsianikov, P. Dubruel, S. Van Vlierberghe, (Photo-)crosslinkable Gelatin Derivatives for Biofabrication applications, Acta Biomater 97 (2019) 46–73. https://doi.org/10.1016/j.actbio.2019.07.035.

[14] S. Bertlein, G. Brown, K.S. Lim, T. Jungst, T. Boeck, T. Blunk, J. Tessmar, G.J. Hooper, T.B.F. Woodfield, J. Groll, Thiol – Ene Clickable Gelatin : A Platform Bioink for Multiple 3D Biofabrication Technologies, Advanced Materials 1703404 (2017) 1–6. https://doi.org/10.1002/adma.201703404.

[15] J. Van Hoorick, A. Dobos, M. Markovic, T. Gheysens, L. Van Damme, P. Gruber, L. Tytgat, J. Van Erps, H. Thienpont, P. Dubruel, A. Ovsianikov, S. Van Vlierberghe, J. Van Hoorick, Thiol-Norbornene gelatin hydrogels: influence of thiolated crosslinker on network properties and high definition 3D printing, Biofabrication (2020). http://iopscience.iop.org/article/10.1088/1758-5090/abc95f.

[16] J. Van Hoorick, P. Gruber, M. Markovic, M. Rollot, G.J. Graulus, M. Vagenende, M. Tromayer, J. Van Erps, H. Thienpont, J.C. Martins, S. Baudis, A. Ovsianikov, P. Dubruel, S. Van Vlierberghe, Highly Reactive Thiol-Norbornene Photo-Click Hydrogels: Toward Improved Processability, Macromol Rapid Commun 39 (2018) 1–7. https://doi.org/10.1002/marc.201800181.

[17] S. Stichler, S. Bertlein, J. Tessmar, T. Jüngst, J. Groll, Thiol-ene Cross-Linkable Hydrogels as Bioinks for Biofabrication, Macromol Symp 372 (2017). https://doi.org/10.1002/masy.201600173.

[18] D. Nieto, J.A. Marchal Corrales, A. Jorge De Mora, L. Moroni, Fundamentals of light-cell-polymer interactions in photo-cross-linking based bioprinting, APL Bioeng 4 (2020). https://doi.org/10.1063/5.0022693.

[19] C.C. Cook, E.J. Fong, J.J. Schwartz, D.H. Porcincula, A.C. Kaczmarek, J.S. Oakdale, B.D. Moran, K.M. Champley, C.M. Rackson, A. Muralidharan, R.R. McLeod, M. Shusteff, Highly Tunable Thiol-Ene Photoresins for Volumetric Additive Manufacturing, Advanced Materials 32 (2020). https://doi.org/10.1002/adma.202003376.

[20] K. Elkhoury, M. Morsink, L. Sanchez-Gonzalez, C. Kahn, A. Tamayol, E. Arab-Tehrany, Biofabrication of natural hydrogels for cardiac, neural, and bone Tissue engineering Applications, Bioact Mater 6 (2021). https://doi.org/10.1016/j.bioactmat.2021.03.040.

[21] L. Parmentier, S. D'Haese, J. Duquesne, F. Bray, L. Van der Meeren, A.G. Skirtach, C. Rolando, R.I. Dmitriev, S. Van Vlierberghe, 2D fibrillar osteoid niche mimicry through inclusion of visco-elastic and topographical cues in gelatin-based networks, Int J Biol Macromol 254 (2024) 127619. https://doi.org/10.1016/j.ijbiomac.2023.127619.

[22] J. Gao, X. Yu, X. Wang, Y. He, J. Ding, Biomaterial–Related Cell Microenvironment in Tissue Engineering and Regenerative Medicine, Engineering 13 (2022) 31–45. https://doi.org/10.1016/j.eng.2021.11.025.

[23] S. Martino, F. D'Angelo, I. Armentano, J.M. Kenny, A. Orlacchio, Stem cell-biomaterial interactions for regenerative medicine, Biotechnol Adv 30 (2012). https://doi.org/10.1016/j.biotechadv.2011.06.015.

[24] L. Xiao, Y. Sun, L. Liao, X. Su, Response of mesenchymal stem cells to surface topography of scaffolds and the underlying mechanisms, J Mater Chem B 11 (2023). https://doi.org/10.1039/d2tb01875f.

[25] V.V. Hiew, S.F.B. Simat, P.L. Teoh, The Advancement of Biomaterials in Regulating Stem Cell Fate, Stem Cell Rev Rep 14 (2018). https://doi.org/10.1007/s12015-017-9764-y.

[26] D.K. Mills, Y. Luo, A. Elumalai, S. Esteve, S. Karnik, S. Yao, Creating structured hydrogel microenvironments for regulating stem cell differentiation, Gels 6 (2020). https://doi.org/10.3390/gels6040047.

[27] M.A. Mohamed, A. Fallahi, A.M.A. El-Sokkary, S. Salehi, M.A. Akl, A. Jafari, A. Tamayol, H. Fenniri, A. Khademhosseini, S.T. Andreadis, C. Cheng, Stimuli-responsive hydrogels for manipulation of cell microenvironment: From chemistry to biofabrication technology, Prog Polym Sci 98 (2019). https://doi.org/10.1016/j.progpolymsci.2019.101147.

[28] G.M. Harris, M.E. Piroli, E. Jabbarzadeh, Deconstructing the Effects of Matrix Elasticity and Geometry in Mesenchymal Stem Cell Lineage Commitment, Adv Funct Mater 24 (2014) 2396–2403. https://doi.org/10.1002/adfm.201303400.

[29] K. Yang, K. Jung, E. Ko, J. Kim, K.I. Park, J. Kim, S.-W. Cho, Nanotopographical Manipulation of Focal Adhesion Formation for Enhanced Differentiation of Human Neural Stem Cells, ACS Appl Mater Interfaces 5 (2013) 10529–10540. https://doi.org/10.1021/am402156f.

[30] L. Parmentier, S. D'Haese, N. Carpentier, R.I. Dmitriev, S. Van Vlierberghe, Bottom-Up Extrusion-Based Biofabrication of the Osteoid Niche, Macromol Biosci 24 (2024). https://doi.org/10.1002/mabi.202300395.

[31] W.L. Murphy, T.C. McDevitt, A.J. Engler, Materials as stem cell regulators, Nat Mater 13 (2014) 547–557. https://doi.org/10.1038/nmat3937.

[32] A.K. Whitehead, H.H. Barnett, M.E. Caldorera-Moore, J.J. Newman, Poly (ethylene glycol) hydrogel elasticity influences human mesenchymal stem cell behavior, Regen Biomater 5 (2018). https://doi.org/10.1093/RB/RBY008.

[33] S. Nellinger, P.J. Kluger, How Mechanical and Physicochemical Material Characteristics Influence Adipose-Derived Stem Cell Fate, Int J Mol Sci 24 (2023). https://doi.org/10.3390/ijms24043551.

[34] O. Chaudhuri, L. Gu, D. Klumpers, M. Darnell, S.A. Bencherif, J.C. Weaver, N. Huebsch, H.P. Lee, E. Lippens, G.N. Duda, D.J. Mooney, Hydrogels with tunable stress relaxation regulate stem cell fate and activity, Nat Mater 15 (2016). https://doi.org/10.1038/nmat4489.

[35] M. Meeremans, L. Van Damme, W. De Spiegelaere, S. Van Vlierberghe, C. De Schauwer, Equine tenocyte seeding on gelatin hydrogels improves elongated morphology, Polymers (Basel) 13 (2021). https://doi.org/10.3390/polym13050747.

[36] N. Pien, F. Bray, T. Gheysens, L. Tytgat, C. Rolando, D. Mantovani, P. Dubruel, S. Van Vlierberghe, Proteomics as a tool to gain next level insights into photo-crosslinkable biopolymer modifications, Bioact Mater 17 (2022) 204–220. https://doi.org/10.1016/j.bioactmat.2022.01.023.

[37] B.D. Fairbanks, M.P. Schwartz, C.N. Bowman, K.S. Anseth, Photoinitiated polymerization of PEG-diacrylate with lithium phenyl-2,4,6-trimethylbenzoylphosphinate: polymerization rate and cytocompatibility, Biomaterials 30 (2009) 6702–6707. https://doi.org/10.1016/j.biomaterials.2009.08.055.

[38] A. Szabó, K. Kolouchova, L. Parmentier, V. Herynek, O. Groborz, S. Van Vlierberghe, Digital Light Processing of 19F MRI-Traceable Gelatin-Based Biomaterial Inks towards Bone Tissue Regeneration, Materials 17 (2024) 2996. https://doi.org/10.3390/ma17122996.

[39] P.N. Bernal, M. Bouwmeester, J. Madrid-Wolff, M. Falandt, S. Florczak, N.G. Rodriguez, Y. Li, G. Größbacher, R. Samsom, M. van Wolferen, L.J.W. van der Laan, P. Delrot, D. Loterie, J. Malda, C. Moser, B. Spee, R. Levato, Volumetric Bioprinting of Organoids and Optically Tuned Hydrogels to Build Liver-Like Metabolic Biofactories, Advanced Materials 34 (2022). https://doi.org/10.1002/adma.202110054.

[40] S. You, Y. Xiang, H.H. Hwang, D.B. Berry, W. Kiratitanaporn, J. Guan, E. Yao, M. Tang, Z. Zhong, X. Ma, D. Wangpraseurt, Y. Sun, T. Lu, S. Chen, High cell density and high-

resolution 3D bioprinting for fabricating vascularized tissues, Sci Adv 9 (2023). https://doi.org/10.1126/sciadv.ade7923.

[41] L. Van Damme, J. Van Hoorick, P. Blondeel, S. Van Vlierberghe, Toward Adipose Tissue Engineering Using Thiol-Norbornene Photo-Crosslinkable Gelatin Hydrogels, Biomacromolecules 22 (2021). https://doi.org/10.1021/acs.biomac.1c00189.

[42] J. Madrid-Wolff, J. Toombs, R. Rizzo, P.N. Bernal, D. Porcincula, R. Walton, B. Wang, F. Kotz-Helmer, Y. Yang, D. Kaplan, Y.S. Zhang, M. Zenobi-Wong, R.R. McLeod, B. Rapp, J. Schwartz, M. Shusteff, H. Talyor, R. Levato, C. Moser, A review of materials used in tomographic volumetric additive manufacturing, MRS Commun 13 (2023) 764–785. https://doi.org/10.1557/s43579-023-00447-x.

[43] C.E. Hoyle, C.N. Bowman, Thiol-Ene Click Chemistry, Angewandte Chemie International Edition 49 (2010) 1540–1573. https://doi.org/10.1002/anie.200903924.

[44] C. Lin, E. Frahm, F.O. Afolabi, Orthogonally Crosslinked Gelatin-Norbornene Hydrogels for Biomedical Applications, Macromol Biosci 24 (2024). https://doi.org/10.1002/mabi.202300371.

[45] H. Shih, T. Greene, M. Korc, C.-C. Lin, Modular and Adaptable Tumor Niche Prepared from Visible Light Initiated Thiol-Norbornene Photopolymerization, Biomacromolecules 17 (2016) 3872–3882. https://doi.org/10.1021/acs.biomac.6b00931.

[46] V. Burchak, F. Koch, L. Siebler, S. Haase, V.K. Horner, X. Kempter, G.B. Stark, U. Schepers, A. Grimm, S. Zimmermann, P. Koltay, S. Strassburg, G. Finkenzeller, F. Simunovic, F. Lampert, Evaluation of a Novel Thiol–Norbornene-Functionalized Gelatin Hydrogel for Bioprinting of Mesenchymal Stem Cells, Int J Mol Sci 23 (2022) 7939. https://doi.org/10.3390/ijms23147939.

[47] J. Carthew, I. Donderwinkel, S. Shrestha, V.X. Truong, J.S. Forsythe, J.E. Frith, In situ miRNA delivery from a hydrogel promotes osteogenesis of encapsulated mesenchymal stromal cells, Acta Biomater 101 (2020) 249–261. https://doi.org/10.1016/j.actbio.2019.11.016.

[48] Y.S. Pek, A.C.A. Wan, J.Y. Ying, The effect of matrix stiffness on mesenchymal stem cell differentiation in a 3D thixotropic gel, Biomaterials 31 (2010) 385–391. https://doi.org/10.1016/j.biomaterials.2009.09.057.

[49] S. Tan, J.Y. Fang, Z. Yang, M.E. Nimni, B. Han, The synergetic effect of hydrogel stiffness and growth factor on osteogenic differentiation, Biomaterials 35 (2014) 5294–5306. https://doi.org/10.1016/j.biomaterials.2014.02.040.

[50] S. Stichler, T. Böck, N. Paxton, S. Bertlein, R. Levato, V. Schill, W. Smolan, J. Malda, J. Teßmar, T. Blunk, J. Groll, Double printing of hyaluronic acid/poly(glycidol) hybrid hydrogels with poly(ϵ-caprolactone) for MSC chondrogenesis, Biofabrication 9 (2017). https://doi.org/10.1088/1758-5090/aa8cb7.

[51] Y. Zhou, J. Qiu, L. Wan, J. Li, The effect of matrix stiffness on the chondrogenic differentiation of mesenchymal stem cells, J Mol Histol 53 (2022) 805–816. https://doi.org/10.1007/s10735-022-10094-6.

[52] D.J. Huey, J.C. Hu, K.A. Athanasiou, Unlike Bone, Cartilage Regeneration Remains Elusive, Science (1979) 338 (2012) 917–921. https://doi.org/10.1126/science.1222454.

[53] S. Musah, S.A. Morin, P.J. Wrighton, D.B. Zwick, S. Jin, L.L. Kiessling, Glycosaminoglycan-Binding Hydrogels Enable Mechanical Control of Human Pluripotent Stem Cell Self-Renewal, ACS Nano 6 (2012) 10168–10177. https://doi.org/10.1021/nn3039148.

[54] D.A. Young, Y.S. Choi, A.J. Engler, K.L. Christman, Stimulation of adipogenesis of adult adipose-derived stem cells using substrates that mimic the stiffness of adipose tissue, Biomaterials 34 (2013) 8581–8588. https://doi.org/10.1016/j.biomaterials.2013.07.103.

[55] K.S. Lim, B.J. Klotz, G.C.J. Lindberg, F.P.W. Melchels, G.J. Hooper, J. Malda, D. Gawlitta, T.B.F. Woodfield, Visible Light Cross-Linking of Gelatin Hydrogels Offers an Enhanced Cell Microenvironment with Improved Light Penetration Depth, Macromol Biosci 19 (2019). https://doi.org/10.1002/mabi.201900098.

[56] Y. Zhu, J. Chen, H. Liu, W. Zhang, Photo-cross-linked Hydrogels for Cartilage and Osteochondral Repair, ACS Biomater Sci Eng (2023). https://doi.org/10.1021/acsbiomaterials.3c01132.

[57] B. Trappmann, J.E. Gautrot, J.T. Connelly, D.G.T. Strange, Y. Li, M.L. Oyen, M.A. Cohen Stuart, H. Boehm, B. Li, V. Vogel, J.P. Spatz, F.M. Watt, W.T.S. Huck, Extracellular-matrix tethering regulates stem-cell fate, Nat Mater 11 (2012) 642–649. https://doi.org/10.1038/nmat3339.

[58] X. Hu, L. Ma, C. Wang, C. Gao, Gelatin Hydrogel Prepared by Photo-initiated Polymerization and Loaded with TGF-β1 for Cartilage Tissue Engineering, Macromol Biosci 9 (2009) 1194–1201. https://doi.org/10.1002/mabi.200900275.

[59] F. Liu, X. Wang, Y. Li, M. Ren, P. He, L. Wang, J. Xu, S. Yang, P. Ji, Dendrimer-modified gelatin methacrylate hydrogels carrying adipose-derived stromal/stem cells promote cartilage regeneration, Stem Cell Res Ther 13 (2022) 26. https://doi.org/10.1186/s13287-022-02705-6.

[60] N. Annabi, A. Tamayol, J.A. Uquillas, M. Akbari, L.E. Bertassoni, C. Cha, G. Camci-Unal, M.R. Dokmeci, N.A. Peppas, A. Khademhosseini, 25th Anniversary Article: Rational Design and Applications of Hydrogels in Regenerative Medicine, Advanced Materials 26 (2014) 85–124. https://doi.org/10.1002/adma.201303233.

[61] C. Yu, K.L. Miller, J. Schimelman, P. Wang, W. Zhu, X. Ma, M. Tang, S. You, D. Lakshmipathy, F. He, S. Chen, A sequential 3D bioprinting and orthogonal bioconjugation approach for precision tissue engineering, Biomaterials 258 (2020) 120294. https://doi.org/10.1016/j.biomaterials.2020.120294.

[62] P.N. Bernal, P. Delrot, D. Loterie, Y. Li, J. Malda, C. Moser, R. Levato, Volumetric Bioprinting of Complex Living-Tissue Constructs within Seconds, Advanced Materials 31 (2019). https://doi.org/10.1002/adma.201904209.

[63] S. Jing, L. Lian, Y. Hou, Z. Li, Z. Zheng, G. Li, G. Tang, G. Xie, M. Xie, Advances in volumetric bioprinting, Biofabrication 16 (2024) 012004. https://doi.org/10.1088/1758-5090/ad0978.

[64] J. Gehlen, W. Qiu, G.N. Schädli, R. Müller, X.-H. Qin, Tomographic volumetric bioprinting of heterocellular bone-like tissues in seconds, Acta Biomater 156 (2023) 49–60. https://doi.org/10.1016/j.actbio.2022.06.020.

[65] R. Rizzo, D. Ruetsche, H. Liu, M. Zenobi-Wong, Optimized Photoclick (Bio)Resins for Fast Volumetric Bioprinting, Advanced Materials 33 (2021). https://doi.org/10.1002/adma.202102900.

[66] P. Chansoria, D. Rütsche, A. Wang, H. Liu, D. D'Angella, R. Rizzo, A. Hasenauer, P. Weber, W. Qiu, N.B.M. Ibrahim, N. Korshunova, X. Qin, M. Zenobi-Wong, Synergizing Algorithmic Design, Photoclick Chemistry and Multi-Material Volumetric Printing for Accelerating Complex Shape Engineering, Advanced Science 10 (2023). https://doi.org/10.1002/advs.202300912.

[67] G. Größbacher, M. Bartolf-Kopp, C. Gergely, P.N. Bernal, S. Florczak, M. de Ruijter, N.G. Rodriguez, J. Groll, J. Malda, T. Jungst, R. Levato, Volumetric Printing Across Melt Electrowritten Scaffolds Fabricates Multi-Material Living Constructs with Tunable Architecture and Mechanics, Advanced Materials 35 (2023). https://doi.org/10.1002/adma.202300756.

[68] K.S. Lim, B.J. Klotz, G.C.J. Lindberg, F.P.W. Melchels, G.J. Hooper, J. Malda, D. Gawlitta, T.B.F. Woodfield, Visible Light Cross-Linking of Gelatin Hydrogels Offers an Enhanced Cell Microenvironment with Improved Light Penetration Depth, Macromol Biosci 19 (2019). https://doi.org/10.1002/mabi.201900098.

[69] T. Kushibiki, Y. Mayumi, E. Nakayama, R. Azuma, K. Ojima, A. Horiguchi, M. Ishihara, Photocrosslinked gelatin hydrogel improves wound healing and skin flap survival by the sustained release of basic fibroblast growth factor, Sci Rep 11 (2021) 23094. https://doi.org/10.1038/s41598-021-02589-1.

[70] M. Guven, K. Barnouin, A.P. Snijders, P. Karran, Photosensitized UVA-Induced Cross-Linking between Human DNA Repair and Replication Proteins and DNA Revealed by Proteomic Analysis, J Proteome Res 15 (2016) 4612–4623. https://doi.org/10.1021/acs.jproteome.6b00717.

[71] R. Masuma, S. Kashima, M. Kurasaki, T. Okuno, Effects of UV wavelength on cell damages caused by UV irradiation in PC12 cells, J Photochem Photobiol B 125 (2013) 202–208. https://doi.org/10.1016/j.jphotobiol.2013.06.003.

[72] D. Ribezzi, M. Gueye, S. Florczak, F. Dusi, D. de Vos, F. Manente, A. Hierholzer, M. Fussenegger, M. Caiazzo, T. Blunk, J. Malda, R. Levato, Shaping Synthetic Multicellular and Complex Multimaterial Tissues via Embedded Extrusion-Volumetric Printing of Microgels, Advanced Materials 35 (2023). https://doi.org/10.1002/adma.202301673.

[73] M. Falandt, P.N. Bernal, O. Dudaryeva, S. Florczak, G. Größbacher, M. Schweiger, A. Longoni, C. Greant, M. Assunção, O. Nijssen, S. van Vlierberghe, J. Malda, T. Vermonden, R. Levato, Spatial-Selective Volumetric 4D Printing and Single-Photon Grafting of Biomolecules within Centimeter-Scale Hydrogels via Tomographic Manufacturing, Adv Mater Technol 8 (2023). https://doi.org/10.1002/admt.202300026.

[74] L. Parmentier, Capturing the biophysical cues of the vascularised bone extracellular matrix to stimulate its regeneration, Ghent University, 2024.

[75] S. You, Y. Xiang, H.H. Hwang, D.B. Berry, W. Kiratitanaporn, J. Guan, E. Yao, M. Tang, Z. Zhong, X. Ma, D. Wangpraseurt, Y. Sun, T. Lu, S. Chen, High cell density and high-resolution 3D bioprinting for fabricating vascularized tissues, Sci Adv 9 (2023). https://doi.org/10.1126/sciadv.ade7923.

[76] P.Y. Liu, L.K. Chin, W. Ser, H.F. Chen, C.-M. Hsieh, C.-H. Lee, K.-B. Sung, T.C. Ayi, P.H. Yap, B. Liedberg, K. Wang, T. Bourouina, Y. Leprince-Wang, Cell refractive index for cell biology and disease diagnosis: past, present and future, Lab Chip 16 (2016) 634–644. https://doi.org/10.1039/C5LC01445J.

[77] T. Boothe, L. Hilbert, M. Heide, L. Berninger, W.B. Huttner, V. Zaburdaev, N.L. Vastenhouw, E.W. Myers, D.N. Drechsel, J.C. Rink, A tunable refractive index matching medium for live imaging cells, tissues and model organisms, Elife 6 (2017). https://doi.org/10.7554/eLife.27240.

[78] P.N. Bernal, M. Bouwmeester, J. Madrid-Wolff, M. Falandt, S. Florczak, N.G. Rodriguez, Y. Li, G. Größbacher, R. Samsom, M. van Wolferen, L.J.W. van der Laan, P. Delrot, D. Loterie, J. Malda, C. Moser, B. Spee, R. Levato, Volumetric Bioprinting of Organoids and Optically Tuned Hydrogels to Build Liver-Like Metabolic Biofactories, Advanced Materials 34 (2022). https://doi.org/10.1002/adma.202110054.

[79] S. Asim, T.A. Tabish, U. Liaqat, I.T. Ozbolat, M. Rizwan, Advances in Gelatin Bioinks to Optimize Bioprinted Cell Functions, Adv Healthc Mater 12 (2023). https://doi.org/10.1002/adhm.202203148.

[80] J.W. Tashman, D.J. Shiwarski, B. Coffin, A. Ruesch, F. Lanni, J.M. Kainerstorfer, A.W. Feinberg, In situ volumetric imaging and analysis of FRESH 3D bioprinted constructs using optical coherence tomography, Biofabrication 15 (2023) 014102. https://doi.org/10.1088/1758-5090/ac975e.

[81] Y. Ding, R. Fu, C.P. Collins, S. Yoda, C. Sun, G.A. Ameer, 3D-Printed Radiopaque Bioresorbable Stents to Improve Device Visualization, Adv Healthc Mater 11 (2022). https://doi.org/10.1002/adhm.202201955.

[82] M. Kirsch, J. Rach, W. Handke, A. Seltsam, I. Pepelanova, S. Strauß, P. Vogt, T. Scheper, A. Lavrentieva, Comparative Analysis of Mesenchymal Stem Cell Cultivation in Fetal Calf Serum, Human Serum, and Platelet Lysate in 2D and 3D Systems, Front Bioeng Biotechnol 8 (2021). https://doi.org/10.3389/fbioe.2020.598389.

[83] I. Osama, N. Gorenkova, C.M. McKittrick, T. Wongpinyochit, A. Goudie, F.P. Seib, H.V.O. Carswell, In vitro studies on space-conforming self-assembling silk hydrogels as a mesenchymal stem cell-support matrix suitable for minimally invasive brain application, Sci Rep 8 (2018) 13655. https://doi.org/10.1038/s41598-018-31905-5.

[84] O. Petrenko, O. Rogulska, N. Trufanova, O. Trufanov, O. Hubenia, O. Revenko, D. Cherkashina, Modulation of mesenchymal stromal cells properties by the microenvironment in 3D culture, ScienceRise: Biological Science (2023) 28–33. https://doi.org/10.15587/2519-8025.2023.288082.

[85] Y. He, F. Yang, H. Zhao, Q. Gao, B. Xia, J. Fu, Research on the printability of hydrogels in 3D bioprinting, Sci Rep 6 (2016) 29977. https://doi.org/10.1038/srep29977.

[86] A.J. Engler, S. Sen, H.L. Sweeney, D.E. Discher, Matrix Elasticity Directs Stem Cell Lineage Specification, Cell 126 (2006) 677–689. https://doi.org/10.1016/j.cell.2006.06.044.

[87] G. Gillispie, P. Prim, J. Copus, J. Fisher, A.G. Mikos, J.J. Yoo, A. Atala, S.J. Lee, Assessment methodologies for extrusion-based bioink printability, Biofabrication 12 (2020) 022003. https://doi.org/10.1088/1758-5090/ab6f0d.

[88] D.F. Duarte Campos, A. Blaeser, A. Korsten, S. Neuss, J. Jäkel, M. Vogt, H. Fischer, The Stiffness and Structure of Three-Dimensional Printed Hydrogels Direct the Differentiation of Mesenchymal Stromal Cells Toward Adipogenic and Osteogenic Lineages, Tissue Eng Part A 21 (2015) 740–756. https://doi.org/10.1089/ten.tea.2014.0231.

[89] C.A. Mullen, T.J. Vaughan, K.L. Billiar, L.M. McNamara, The Effect of Substrate Stiffness, Thickness, and Cross-Linking Density on Osteogenic Cell Behavior, Biophys J 108 (2015) 1604–1612. https://doi.org/10.1016/j.bpj.2015.02.022.

[90] M. Kamaraj, G. Sreevani, G. Prabusankar, S.N. Rath, Mechanically tunable photo-cross-linkable bioinks for osteogenic differentiation of MSCs in 3D bioprinted constructs, Materials Science and Engineering: C 131 (2021) 112478. https://doi.org/10.1016/j.msec.2021.112478.

[91] X. Liu, Y. Wang, Y. He, X. Wang, R. Zhang, A. Bachhuka, R. Madathiparambil Visalakshan, Q. Feng, K. Vasilev, Synergistic Effect of Surface Chemistry and Surface Topography Gradient on Osteogenic/Adipogenic Differentiation of hMSCs, ACS Appl Mater Interfaces 13 (2021) 30306–30316. https://doi.org/10.1021/acsami.1c03915.

[92] L. Yang, L. Ge, P. van Rijn, Synergistic Effect of Cell-Derived Extracellular Matrices and Topography on Osteogenesis of Mesenchymal Stem Cells, ACS Appl Mater Interfaces 12 (2020) 25591–25603. https://doi.org/10.1021/acsami.0c05012.

[93] M.-H. You, M.K. Kwak, D.-H. Kim, K. Kim, A. Levchenko, D.-Y. Kim, K.-Y. Suh, Synergistically Enhanced Osteogenic Differentiation of Human Mesenchymal Stem Cells by Culture on Nanostructured Surfaces with Induction Media, Biomacromolecules 11 (2010) 1856–1862. https://doi.org/10.1021/bm100374n.

[94] A. Prosser, C. Scotchford, G. Roberts, D. Grant, V. Sottile, Integrated Multi-Assay Culture Model for Stem Cell Chondrogenic Differentiation, Int J Mol Sci 20 (2019) 951. https://doi.org/10.3390/ijms20040951.

[95] A. Barlian, H. Judawisastra, N.M. Alfarafisa, U.A. Wibowo, I. Rosadi, Chondrogenic differentiation of adipose-derived mesenchymal stem cells induced by L-ascorbic acid and platelet rich plasma on silk fibroin scaffold, PeerJ 6 (2018) e5809. https://doi.org/10.7717/peerj.5809.

[96] K.C. Russell, D.G. Phinney, M.R. Lacey, B.L. Barrilleaux, K.E. Meyertholen, K.C. O'Connor, In Vitro High-Capacity Assay to Quantify the Clonal Heterogeneity in Trilineage Potential of Mesenchymal Stem Cells Reveals a Complex Hierarchy of Lineage Commitment, Stem Cells 28 (2010) 788–798. https://doi.org/10.1002/stem.312.

[97] E. Heyman, M. Meeremans, B. Devriendt, M. Olenic, K. Chiers, C. De Schauwer, Validation of a color deconvolution method to quantify MSC tri-lineage differentiation across species, Front Vet Sci 9 (2022). https://doi.org/10.3389/fvets.2022.987045.

[98] A.L. Gale, R.L. Linardi, G. McClung, R.M. Mammone, K.F. Ortved, Comparison of the Chondrogenic Differentiation Potential of Equine Synovial Membrane-Derived and Bone Marrow-Derived Mesenchymal Stem Cells, Front Vet Sci 6 (2019). https://doi.org/10.3389/fvets.2019.00178.

[99] Y. Ohori-Morita, A. Ashry, K. Niibe, H. Egusa, Current perspectives on the dynamic culture of mesenchymal stromal/stem cell spheroids, Stem Cells Transl Med (2024). https://doi.org/10.1093/stcltm/szae093.

[100] K. Sonomoto, K. Yamaoka, H. Kaneko, K. Yamagata, K. Sakata, X. Zhang, M. Kondo, Y. Zenke, K. Sabanai, S. Nakayamada, A. Sakai, Y. Tanaka, Spontaneous Differentiation of Human Mesenchymal Stem Cells on Poly-Lactic-Co-Glycolic Acid Nano-Fiber Scaffold, PLoS One 11 (2016) e0153231. https://doi.org/10.1371/journal.pone.0153231.

[101] D. Bosnakovski, M. Mizuno, G. Kim, T. Ishiguro, M. Okumura, T. Iwanaga, T. Kadosawa, T. Fujinaga, Chondrogenic differentiation of bovine bone marrow mesenchymal stem cells in pellet cultural system, Exp Hematol 32 (2004) 502–509. https://doi.org/10.1016/j.exphem.2004.02.009.

[102] D. Bosnakovski, M. Mizuno, G. Kim, S. Takagi, M. Okumur, T. Fujinag, Gene expression profile of bovine bone marrow mesenchymal stem cell during spontaneous chondrogenic differentiation in pellet culture system., Jpn J Vet Res 53 (2006) 127–39.

[103] R. Goldshmid, H. Simaan-Yameen, L. Ifergan, C. Loebel, J.A. Burdick, D. Seliktar, Modulus-dependent effects on neurogenic, myogenic, and chondrogenic differentiation of human mesenchymal stem cells in three-dimensional hydrogel cultures, J Biomed Mater Res A 111 (2023) 1441–1458. https://doi.org/10.1002/jbm.a.37545.

[104] J.L. Ramirez-Zacarias, F. Castro-Munozledo, W. Kuri-Harcuch, Quantitation of adipose conversion and triglycerides by staining intracytoplasmic lipids with oil red O, Histochemistry 97 (1992) 493–497. https://doi.org/10.1007/BF00316069.

[105] Y. Chen, Q. Li, Y. Liu, X. Chen, S. Jiang, W. Lin, Y. Zhang, R. Liu, B. Shao, C. Chen, Q. Yuan, C. Zhou, AFF4 regulates cellular adipogenic differentiation via targeting autophagy, PLoS Genet 18 (2022) e1010425. https://doi.org/10.1371/journal.pgen.1010425.

[106] Y. Shibaike, K. Sano, M. Gotoh, Endoplasmic reticulum stress inhibits adipocyte differentiation of mesenchymal stem cells, Cytologia (Tokyo) 88 (2023) D-23-00030. https://doi.org/10.1508/cytologia.88.255.

[107] W. Zhao, X. Li, X. Liu, N. Zhang, X. Wen, Effects of substrate stiffness on adipogenic and osteogenic differentiation of human mesenchymal stem cells, Materials Science and Engineering: C 40 (2014) 316–323. https://doi.org/10.1016/j.msec.2014.03.048.

[108] J.S. Park, J.S. Chu, A.D. Tsou, R. Diop, Z. Tang, A. Wang, S. Li, The effect of matrix stiffness on the differentiation of mesenchymal stem cells in response to TGF-β, Biomaterials 32 (2011) 3921–3930. https://doi.org/10.1016/j.biomaterials.2011.02.019.

[109] J.H. Wen, L.G. Vincent, A. Fuhrmann, Y.S. Choi, K.C. Hribar, H. Taylor-Weiner, S. Chen, A.J. Engler, Interplay of matrix stiffness and protein tethering in stem cell differentiation, Nat Mater 13 (2014) 979–987. https://doi.org/10.1038/nmat4051.

[110] V. Burchak, F. Koch, L. Siebler, S. Haase, V.K. Horner, X. Kempter, G.B. Stark, U. Schepers, A. Grimm, S. Zimmermann, P. Koltay, S. Strassburg, G. Finkenzeller, F. Simunovic, F. Lampert, Evaluation of a Novel Thiol–Norbornene-Functionalized Gelatin Hydrogel for Bioprinting of Mesenchymal Stem Cells, Int J Mol Sci 23 (2022) 7939. https://doi.org/10.3390/ijms23147939.

[111] Y. Wu, Z. Yang, J.B.K. Law, A.Y. He, A.A. Abbas, V. Denslin, T. Kamarul, J.H.P. Hui, E.H. Lee, The Combined Effect of Substrate Stiffness and Surface Topography on Chondrogenic Differentiation of Mesenchymal Stem Cells, Tissue Eng Part A 23 (2017) 43–54. https://doi.org/10.1089/ten.tea.2016.0123.

[112] S. Moeinzadeh, S.R. Pajoum Shariati, E. Jabbari, Comparative effect of physicomechanical and biomolecular cues on zone-specific chondrogenic differentiation of mesenchymal stem cells, Biomaterials 92 (2016) 57–70. https://doi.org/10.1016/j.biomaterials.2016.03.034.